Original Research Article

International journal of spray and combustion dynamics

International Journal of Spray and Combustion Dynamics
2016, Vol. 8(2) 119–146
© The Author(s) 2016
Reprints and permissions:
sagepub.co.uk/journalsPermissions.nav
DOI: 10.1177/1756827716651571
scd.sagepub.com

SAGE

Non-normality and nonlinearity in thermoacoustic instabilities

RI Sujith[1], MP Juniper[2] and PJ Schmid[3]

Abstract

Analysis of thermoacoustic instabilities were dominated by modal (eigenvalue) analysis for many decades. Recent progress in nonmodal stability analysis allows us to study the problem from a different perspective, by quantitatively describing the short-term behavior of disturbances. The short-term evolution has a bearing on subcritical transition to instability, known popularly as triggering instability in thermoacoustic parlance. We provide a review of the recent developments in the context of triggering instability. A tutorial for nonmodal stability analysis is provided. The applicability of the tools from nonmodal stability analysis are demonstrated with the help of a simple model of a Rjike tube. The article closes with a brief description of how to characterize bifurcations in thermoacoustic systems.

Keywords

Thermoacoustic instability, non-normality, nonlinearity, transient growth, triggering

Date received: 28 January 2014; accepted: 20 August 2015

Introduction

When Yuri Gagarin was launched into orbit in 1961 on a Vostok 1, the probability of a rocket blowing up on take-off was around 50%.[1] In those days, one of the most persistent causes of failure was a violent oscillation caused by the coupling between acoustics and heat release in the combustion chamber. These thermoacoustic oscillations have caused countless rocket engine and gas turbine failures since the 1930s and have been studied extensively.[2] Nevertheless, they are still one of the major problems facing rocket and gas turbine manufacturers today.[3] A short history of thermoacoustic oscillations in liquid-fueled rockets, gas-fueled rockets, solid-fueled rockets, ramjets, afterburners, and gas turbines can be found in section 1.2 of Culick.[2]

Rockets, jet engines, and power generating gas turbines are particularly susceptible to coupling between heat release and acoustics because they have high energy densities and low acoustic damping. The energy densities are roughly $10\,\mathrm{GW\,m^{-3}}$ for liquid rockets, $1\,\mathrm{GW\,m^{-3}}$ for solid rockets, and $0.1\,\mathrm{GW\,m^{-3}}$ for jet engines and afterburners. The acoustic damping is low because combustion chambers tend to be nearly closed systems whose walls reflect sound. Consequently, high amplitude acoustic oscillations are sustained even when a small proportion of the available thermal energy is converted to acoustic (mechanical) energy. Furthermore, because so much thermal energy is available, the existence and amplitude of thermoacoustic oscillations tend to be very sensitive to small changes in the system and therefore difficult to predict.

Entropy, vortical, and acoustic waves

In order to achieve high energy densities, the combustion inside rocket and jet engines is highly turbulent. It might seem surprising that long wavelength acoustic waves can become so strong, given that the heat release fluctuations associated with turbulent combustion occur on small time and length scales. To explain this, it helps to consider small amplitude perturbations to the flow in a combustor. These can be decomposed into entropy waves (hot spots), vorticity waves, and acoustic waves. These waves interact at boundaries and in the combustion zone. The interaction in the

[1]Department of Aerospace Engineering, Indian Institute of Technology Madras, Chennai, India
[2]Department of Engineering, IIT Madras, Chennai, India
[3]Faculty of Natural Sciences, Department of Mathematics, Imperial College London, London, UK

Corresponding author:
RI Sujith, Department of Aerospace Engineering, Indian Institute of Technology Madras, Chennai, India.
Email: sujith@iitm.ac.in

Creative Commons CC-BY-NC: This article is distributed under the terms of the Creative Commons Attribution-NonCommercial 3.0 License (http://www.creativecommons.org/licenses/by-nc/3.0/) which permits non-commercial use, reproduction and distribution of the work without further permission provided the original work is attributed as specified on the SAGE and Open Access pages (https://us.sagepub.com/en-us/nam/open-access-at-sage).

combustion zone is central to this article. They also interact if the mean flow is not uniform or if perturbations are large enough to be nonlinear.

In order for thermal energy to be converted to mechanical energy, higher heat release must coincide with higher pressure, and lower heat release must coincide with lower pressure. Small entropy and vorticity waves do not cause appreciable pressure perturbations and therefore cannot contribute to this mechanism by themselves. Acoustic waves, however, cause both pressure and velocity perturbations. These perturbations change the entry conditions to the combustor, causing entropy and vorticity fluctuations within the combustor. These then lead to fluctuating heat release, in time with the pressure waves. Thermal energy is thereby converted to mechanical energy, usually building up over many cycles and usually preferring long wavelengths, at which the pressure is more coherent over the combustion zone. This explains why classical acoustic waves are the predominant feature of thermoacoustic oscillations even though combustion chambers contain highly turbulent flow, which comprises predominantly entropy and vorticity waves.

In this article, entropy and vorticity waves will be neglected outside the combustion zone. It is important to recognize, however, that this precludes the study of some influential feedback mechanisms, such as entropy waves passing through a convergent nozzle and radiating pressure waves back into the combustor.[4]

Linear analysis of the steady base flow

The simplest starting point for the study of thermoacoustic oscillations is a linear stability analysis of the steady base flow. This either considers the behavior of perturbations that are periodic in time, or the response to an impulse. In both cases, the system is said to be linearly stable if every small perturbation decays in time and linearly unstable if at least one perturbation grows in time. These analyses have been performed on all types of rocket and gas turbine engines[2] and are used in network models, which predict the stability of industrial gas turbines. Most of the analysis in the last 50 years has been linear.

Nonlinear analysis

If a combustor is linearly unstable, the amplitude of infinitesimal thermoacoustic oscillations grows exponentially until their amplitude becomes so large that nonlinear behavior overwhelms the linear behavior. In the simplest cases, the system reaches a constant amplitude periodic solution. In other cases it can reach multi-periodic, quasi-periodic, intermittent, or chaotic solutions.[5–9]

The operating point at which the combustor transitions from linear stability to linear instability is called a bifurcation point. If the system's behavior around this point is periodic, it is called a Hopf bifurcation. The nonlinear behavior around this point is particularly crucial. On the one hand, if the growth rate decreases as the oscillations' amplitude increases, then the steady state amplitude grows gradually as the operating point passes through the Hopf bifurcation. This is known as a supercritical bifurcation. On the other hand, if the growth rate increases as the oscillations' amplitude increases, then the steady state amplitude runs away as the operating point passes through the Hopf bifurcation point, until a higher order nonlinearity acts to limit it. This is known as a subcritical bifurcation. The range of operating conditions in which the system can support a stable nonoscillating solution and a stable oscillating solution is known as the bistable region. The behavior observed in this region depends on the history of the system. We will return to this in §1.6 and say more about bifurcations in §2.

Sources of nonlinearity

There are three main sources of nonlinearity in combustion systems: (1) nonlinear gas dynamics, which become significant when the velocity of the acoustic perturbations is not small compared with the speed of sound and is quantified by the acoustic Mach number; (2) nonlinear heat release rate, which becomes significant when the velocity of the acoustic perturbations is not small compared with that of the mean flow;[10] (3) nonlinear damping.

Nonlinear gas dynamics are particularly relevant for rocket motors, in which the energy densities are very high and the acoustic Mach number is large.[11–15] An important conclusion of these studies is that systems that have linear heat release rate and nonlinear gas dynamics from first to third order do not exhibit subcritical bifurcations.[16]

As well as in the above references, nonlinear heat release has been examined by Refs.[17–20] Nonlinear heat release rate can cause subcritical bifurcations, whether the gas dynamics are linear or nonlinear. In general, the heat release rate is a function of the velocity and pressure fluctuations. For solid rocket engines, pressure fluctuations have the strongest influence. However, for most other applications, velocity fluctuations have the strongest influence. For these reasons, in this article we will focus on systems with linear acoustics and in which heat release rate is a nonlinear function of velocity.

Nonlinear damping mechanisms have been examined by Matveev,[21] who included the amplitude dependence of acoustic radiation. Nonlinear damping is a very influential factor in the behavior of thermoacoustic systems but is not the subject of this article.

Although much work has been done over the last 50 years, it is mostly in the framework of classical linear stability analysis. A comprehensive prediction of the conditions for the onset of instabilities is a difficult task, which is not yet mastered. In particular, predicting the limit-cycle amplitude of oscillations remains a key challenge because little is known, even in a qualitative sense, about the key parameters controlling nonlinear flame dynamics, even in simple laminar flames.[3]

A simple nonlinear thermoacoustic system

The analysis of transient growth and triggering in the Rijke tube is performed on the Rijke tube, which is a simple thermoacoustic system. This is an open-ended duct, through which air passes, with a heat source located near a quarter length from the end at which air enters. If the duct is vertical, the air can be driven by natural convection. If it is horizontal, the air must be driven by forced convection.

Heckl[22] studied nonlinear effects leading to limit cycles in a Rijke tube, both experimentally and theoretically. She showed that the most influential nonlinear effects are nonlinear heat release rate and nonlinear damping. The former is caused by the reduction of the rate of heat transfer when the velocity amplitudes are of the same order as the mean velocity. The latter is caused by the increase of losses at the ends of the tube at very high amplitudes. Hantschk and Vortmeyer[23] also showed that the limit-cycle amplitude in a Rijke tube is determined by nonlinearities in the heat flux from the heating element to the flow.

In order to explain the nonlinear effects of a Rijke tube, Matveev and Culick[21,24] constructed a simple theory by using an energy approach. The equilibrium states of the system are found by balancing thermoacoustic energy input and acoustic losses. Their work reaffirmed that the nonlinearity of the unsteady heat transfer is a dominant factor in determining the limit-cycle amplitude. Furthermore, Matveev and Culick[25] demonstrated the necessity of accurately modeling the effects of the temperature gradient on the mode shapes to obtain accurate results for stability.

Yoon et al.[26] proposed a nonlinear model of a generalized Rijke tube. Their model for the oscillatory heat release rate was not derived from physical principles. They derived both closed form and numerical solutions for the acoustic field by an approximate modal analysis using a two-mode formulation. The two-mode nonlinear model is capable of predicting the growth of oscillations in an initially decaying system. They refer to this as the bootstrapping effect, which they say characterizes nonlinear velocity sensitive combustion response in rocket motors.

Triggering

The concept of a combustor that can sustain oscillations even when its base flow is linearly stable was introduced in the Introduction for combustors that have a bistable region. The question now is whether the system can be pulsed from the stable base flow to the sustained oscillations, and vice-versa. This is known as ''triggering.''

Between the stable base flow and the sustained limit cycle oscillation, there is an unstable limit cycle. This will be described in more detail in Nonlinearity and bifurcation diagrams. To a first approximation (but only to a first approximation) if a pulse is big enough to force the system beyond the unstable limit cycle, and in the right direction, it will continue to grow to sustained oscillations. Below this amplitude, it will decay back to the stable base flow.[18]

Triggering was first reported in solid rockets in the 1960s.[27] The first analyses were performed by Mitchell et al.[28] and Zinn and Lores.[29] Examples of triggering can be found in Culick[2] (Fig. 7.49) for solid rocket engines and liquid rocket engines and[10] for a model gas turbine combustor.

The pulse that causes triggering can be imposed deliberately, as in tests on the Apollo F1 engine, can be caused by unforeseen events, such as debris exiting the choked nozzle of a solid rocket motor (SRM) during firing or can be caused by background noise levels.[10,30,31] Triggering seems to be common to all types of thermoacoustic system, although probably not to each individual system.

As well as identifying the unstable limit cycle as a threshold for the onset of triggering,[18] also discovered that the phase and frequency content of the initial pulse is influential. In particular, Wicker et al.[18] found that, in order to cause triggering, most of the pulse's energy must be contained in the fundamental acoustic mode. This can be explained by nonlinearity alone. However, the fact that triggering in some systems seems to be provoked by nothing more the background noise, can only be explained by non-normality.

Non-normality

The non-normal nature of themoacoustic oscillations has not received any attention until recently. It is a linear phenomenon and is usually investigated for infinitesimal perturbations around a steady base flow. It can equally well be calculated around periodic solutions, however[32,33] in which case it measures the transient growth of infinitesimal perturbations away from a periodic solution.

Nicoud et al.[34] have shown that the eigenvectors of a general thermoacoustic system are nonorthogonal in the presence of heat release or in the presence of general complex impedance boundary conditions. Systems with nonorthogonal eigenvectors are always non-normal

and this can lead to transient growth of oscillations even when the eigenvalues indicate linear stability.

The role of non-normality in thermoacoustic oscillations has been shown in the context of ducted diffusion flames,[35] the Rijke tube Mariappan and Sujith,[33,36–38] premixed flames,[39] and vortex combustors[40] using a Galerkin type analysis. In more detail, Kedia et al.[41] showed that ignoring the linear coupling of the modes results in significant changes in the linear and nonlinear system dynamics. Mariappan and Sujith[42] investigated non-normality in the context of pulsed instabilities in SRMs. Kulkarni et al.[43] demonstrated that non-normality and transient growth can lead to the failure of traditional controllers that are designed based on classical linear stability analysis.

Recently, Mariappan et al.[44] showed experimentally that the eigenmodes of a horizontal Rijke tube are non-orthogonal. Wieczoerk et al.[45] studied non-normal effects for a thermoacoustic system that contains both a source of entropy fluctuations and a zone of accelerated mean flow. Zhao[46] studied non-normality in a Rijke tube. Kim and Hochgreb[47] studied triggering and transient growth in a model gas turbine combustor. Waugh et al.[48] and Waugh and Juniper[30] numerically and Jagadesan and Sujith[31] experimentally studied noise induced transition to instability and the role played by non-normality in a Rijke tube. Mangesius and Polifke[49] adopted a discrete-time, state-space approach for the investigation of non-normal effects in thermoacoustic systems.

In systems with no bistable region, non-normality is just a curiosity. It increases the rate at which sustained oscillations are reached, but it is not the cause of them being reached. Its only substantial effect is to change a system's sensitivity to external noise.[50]

In systems with a bistable region, however, non-normality plays a critical role in triggering. In the subcritical region, perturbations can grow transiently away from the steady base flow and grow transiently around the unstable periodic solution. This means that non-normality helps triggering to occur from pulses that have less energy than that of the unstable periodic solution. The first clues to this behavior could be found in the observation of Wicker et al.[18] that most of the energy must be in the first mode and that the phase and frequency content of the pulse is critical. The aim of this article is to explain why this is.

In summary, there are two distinct aspects of combustion acoustic interactions: (1) nonlinearity; (2) non-orthogonality of the eigenmodes of the linearized system. The objective of this article is to highlight these aspects, particularly in the context of subcritical bifurcations. The rest of this article is organized as follows. Nonlinearity and bifurcation diagrams are first introduced. Then we present a tutorial on nonmodal stability analysis, together with its consequences in the context of thermoacoustic instabilities. Next, we present a simple "toy model" for a horizontal Rijke tube, which has many features of a thermoacoustic system. Non-normality and its consequences in subcritical transition to instability are then explained, using this model. We then proceed to present studies on transient growth in more complex systems. Finally methodologies to characterize bifurcations, both experimentally and numerically, are presented.

Nonlinearity and bifurcation diagrams

Two systems with the same control parameter, R, are shown in Figure 1 in order to demonstrate two types of bifurcation. In flow instability, R is usually a Reynolds number. In thermoacoustics, R could be a heat release parameter or a geometric quantity such as the position of a flame within a combustion chamber. R is plotted on the horizontal axis and some measure of the amplitude of the system, a, is plotted on the vertical axis. In an oscillating system, this is often the peak-to-peak amplitude of the oscillations.

At low values of R, there is a single solution with zero amplitude, which is called a fixed point. The growth rate of the amplitude of infinitesimal linear perturbations around this fixed point, $(\mathrm{d}a/\mathrm{d}t)/a$, can be calculated, usually by finding the eigenvalues of the associated linear stability operator. If all the eigenvalues are stable then all the infinitesimal perturbations around the fixed point have negative growth rate and the fixed point is stable. An example of a stable fixed point in fluid mechanics is the steady and stable flow around a cylinder at Reynolds number less than 45. An example in thermoacoustics is the Rijke tube whose heater is placed three quarters of a length from the end at which the air enters.

When R reaches R_l, at least one pair of eigenvalues around the fixed point becomes unstable and the amplitude of the infinitesimal perturbations starts to grow exponentially, that is $(\mathrm{d}a/\mathrm{d}t)/a$ is a positive constant. This is the Hopf bifurcation point mentioned in the introduction. The fixed point remains a solution of the governing equations but is unstable, shown by a dashed line in Figure 1. An example of this unstable fixed point is the steady flow around a cylinder at Reynolds numbers above 45 (e.g., Fig. 5 in Giannetti and Luchini[51]). It can be calculated numerically but cannot be achieved experimentally without active control.

As the perturbations grow, nonlinearities become significant and the growth rate, $(\mathrm{d}a/\mathrm{d}t)/a$, becomes a function of a. At a certain amplitude, the growth rate reaches zero and the state reaches a periodic solution, which is also known as a limit cycle. The stability of this solution can be examined by considering the growth rate of infinitesimal perturbations around one period.

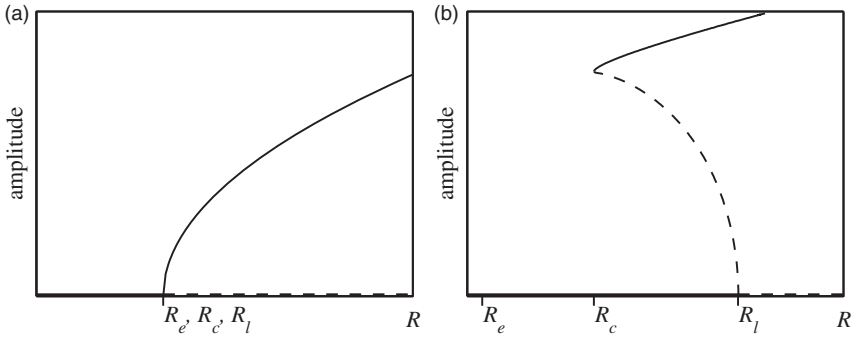


Figure 1. The steady state oscillation amplitude, a_{SS}, as a function of a control parameter, R, for (a) a supercritical bifurcation and (b) a subcritical bifurcation. R_l is the point at which the fixed point (i.e., the zero amplitude solution) becomes unstable. R_c is the point below which no oscillations can be sustained and R_e is the point below which all perturbations decrease monotically to zero.

This is called a Floquet analysis. If all perturbations have negative growth rate then it is stable, shown by solid lines in Figure 1. If at least one perturbation has positive growth rate then it is unstable, shown by dashed lines in Figure 1.

The nonlinear behavior around the Hopf point at R_l is particularly crucial. If the growth rate, $(da/dt)/a$, decreases as a increases then the steady state amplitude of periodic solutions, a_{SS}, is a gradually growing function of R for $R > R_l$. This is known as a supercritical bifurcation (Figure 1(a)). If the growth rate increases as a increases then the amplitude, a, runs away as R increases through the Hopf point until a higher order nonlinearity acts to limit it. In the latter case, there is a periodic solution that continues from the Hopf point, but it lies at $R < R_l$ and it is unstable (Figure 1(b)). This is known as a subcritical bifurcation.

For subcritical bifurcations there is a range of R over which the system can support both a stable fixed point and a stable periodic solution. This range is called the bistable region. It is bounded on one side by the Hopf bifurcation point, R_l, and on the other by the fold point, R_c, below which there are no periodic solutions. The final state of the system at these values of R depends on its history.

The rate of change of energy with time, dE/dt, can also be calculated for the nonlinear system. The maximum value of R that gives $dE/dt < 0$ for all states gives a bound for absolute stability, R_e. Although conceptually useful, this bound is usually not practically useful because it often much smaller than the value at the fold point, R_c. If the linear stability operator is normal and if the nonlinear terms conserve or dissipate energy, then the bifurcation is supercritical and R_e coincides with R_c and R_l. More detail will be given later. Benard convection and Von-Karman vortex shedding are examples of situations in flow instability that become unstable through supercritical bifurcations. In these situations, a linear stability analysis around the fixed point determines R_l, R_e, and R_c accurately.

Periodic solutions and fixed points can be calculated with continuation analysis programs such as AUTO and DDE Biftool. The first example of such tools being applied to thermoacoustics by Jahnke and Culick[52] and they have since been used extensively. Until recently, they have been limited to a few tens of degrees of freedom but systems with several thousand degrees of freedom can be considered now.[53,54]

Periodic solutions are not the only possible solutions to nonlinear differential equations. There can also be multi-periodic, quasi-periodic, and chaotic solutions. These solutions have multiple local peaks at each value of the control parameter R. These types of solution appear in thermoacoustic models such as Figs. 4 and 6 in Sterling and Zukoski [5 and in thermoacoustic experiments such as Gotoda et al.[55] and Kabiraj et al.[7]

Non-normality and transient growth

Principles of nonmodal stability analysis

Nonmodal stability theory is concerned with the accurate quantitative description of disturbance behavior governed by a linear non-normal evolution operator. It has its origin in scientific studies from the late 1980s and early 1990s,[56–62] even though various aspects and features can be traced back to much earlier investigations or observations. Since these early days, nonmodal stability theory has evolved and matured significantly, is now applied rather routinely across a wide range of applications and flow configurations,[63] and has found its place within hydrodynamic stability theory in particular and fluid dynamics in general.[32,64] In its approach, nonmodal stability theory distinguishes itself from the traditional view of assigning significance to individual eigenvalues; rather, it describes the complete dynamics of the flow as a superposition of many eigensolutions.

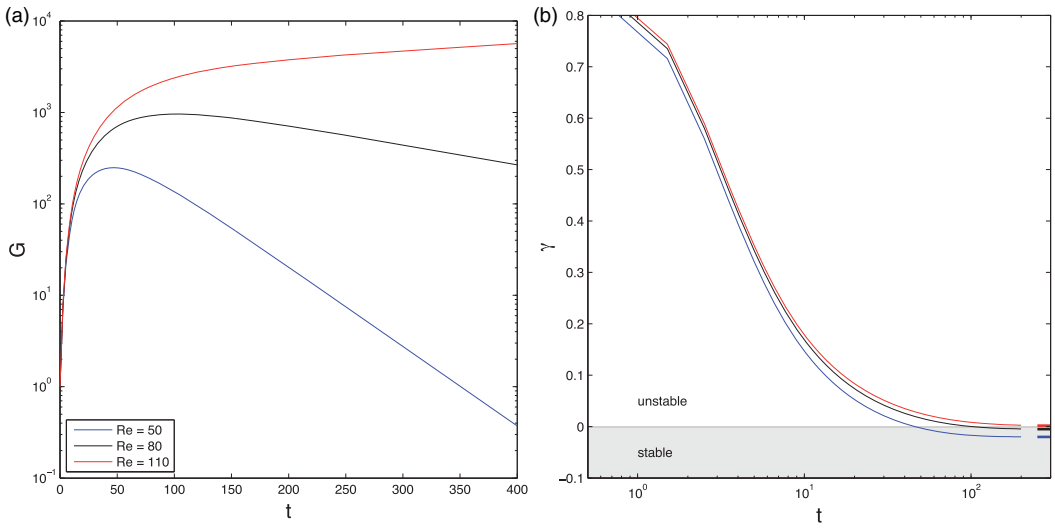


Figure 2. (a) Energy amplification versus time for the LTI system (equation (1)) for three selected Reynolds numbers. (b) Instantaneous energy growth rates for the three cases. The asymptotic energy growth rates are indicated on the right edge of the figure by thick line segments.

In this superposition the decay/growth and oscillatory characteristics (given by the eigenvalues) are as important as the angle between the individual eigenfunctions. In what follows we will give a basic introduction to fundamental concepts underlying nonmodal stability analysis. Particularly, we will demonstrate these concepts on rather small model-systems; this approach should make the essential components of nonmodal analysis more transparent and lay the foundation for applications to systems with more degrees of freedom and more complex behavior.

Linear analysis of non-normal systems. The simplest category of governing equations is given by the class of linear time-invariant (LTI) systems which can simply be described by the temporal evolution equation

$$\frac{d}{dt}\mathbf{q} = \mathsf{A}\mathbf{q} \qquad \mathbf{q}(0) = \mathbf{q}_0 \tag{1}$$

where the matrix A stands for the spatially discretized governing equations and $\mathbf{q}$ denotes the spatially discretized state-vector describing the flow disturbance. An even more drastic simplication is the reduction to only two degrees of freedom resulting in an evolution equation of the form

$$\frac{d}{dt}\begin{pmatrix} q_1 \\ q_2 \end{pmatrix} = \begin{pmatrix} \frac{1}{100} - \frac{1}{Re} & 1 \\ 0 & -\frac{2}{Re} \end{pmatrix}\begin{pmatrix} q_1 \\ q_2 \end{pmatrix} \tag{2}$$

together with appropriate initial conditions. A parameter Re has been introduced to mimic the dependence on a Reynolds number. The particular form of the system matrix A allows us to determine the eigenvalues of the system as $\lambda_1 = 1/100 - 1/Re$ and $\lambda_2 = -2/Re$; the first one changes sign at a critical value of the Reynolds number ($Re_{crit} = 100$), the second one is always negative. For Reynolds numbers $Re < 100$ we thus have a stable system.

Taking a more general (less asymptotic) approach to stability theory, we are interested in the maximum temporal amplification $G(t)$ of perturbation energy governed by equation (2) over a *finite* time span t. Mathematically, this amounts to[63,64]

$$G(t) = \max_{\mathbf{q}_0} \frac{\|\mathbf{q}(t)\|^2}{\|\mathbf{q}_0\|^2} = \max_{\mathbf{q}_0} \frac{\|\exp(t\mathsf{A})\mathbf{q}_0\|^2}{\|\mathbf{q}_0\|^2} = \|\exp(t\mathsf{A})\|^2 \tag{3}$$

where the square of the norm of the state vector $\mathbf{q}$ symbolizes the kinetic energy of the disturbance. In the above expression we have used the matrix exponential $\exp(t\mathsf{A})$ as the formal solution of equation (2) as well as the definition of an induced matrix norm. The quantity $G(t)$ then describes the largest possible energy amplification of *any* initial condition over a time interval $[0, t]$.

Figure 2(a) shows the maximum energy amplification $G(t)$ versus time for three selected Reynolds numbers. Short-time energy growth is observed, before $G(t)$ approaches the exponentially decaying (for $Re = 50, 80$) or growing (for $Re = 110$) behavior one would expect from inspection of the eigenvalues. The instantaneous energy growth rate defined as $\gamma(t) = \frac{1}{E}\frac{dE}{dt}$ with $E = \|\mathbf{q}\|^2 = \langle \mathbf{q}, \mathbf{q} \rangle$ is given in Figure 2(b) for the same three Reynolds numbers, with the asymptotic values

indicated on the right edge of the figure by the thick colored lines. Again, we observe substantial positive energy growth rates for short times, before the asymptotic values are approached.

To better understand this behavior, a geometric point of view is taken.[32] The solution to the initial value problem, equation (2) may be expanded in terms of the eigenvalues $\lambda_{1,2}$ and eigenvectors $\Phi_{1,2}$ of the 2×2 evolution matrix A according to

$$\mathbf{q} = c_1 \Phi_1 \exp((1/100 - 1/Re)t) + c_2 \Phi_2 \exp(-2t/Re) \tag{4}$$

with the coefficients $c_{1,2}$ given by the initial condition. It is easily verified that the two eigenvectors are non-orthogonal (under the standard inner product); in fact, the scalar product of Φ_1 and Φ_2 approaches $\cos\theta = 100/\sqrt{10001}$, that is, the eigenvectors become nearly colinear ($\theta = 0.573^{\circ}$) as the Reynolds number tends to infinity. As a consequence, the coefficients $c_{1,2}$ may be substantially larger in magnitude than the norm of the initial condition we wish to express. For example, for large Reynolds numbers, the initial state vector $\mathbf{q} = [0, 1]^T$ would require $c_1 \sim 100$ and $c_2 \sim -\sqrt{10001}$, and the two components in equation (4) will cancel each other to result in a unit-norm initial condition. As time progresses, this mutual cancellation ceases to hold which subsequently gives rise to state vectors with large norms (or flow states with large energies) before asymptotic decay/growth eventually sets in.

This type of behavior is illustrated in Figure 3. For the non-normal case (on the right), we observe that two large, nonorthogonal vectors, that nearly cancel, are required to produce the initial condition (indicated by the thick blue line). We further assume that the decay along one of the vectors is more rapid (green symbols) than along the other one (red symbols). The nonorthogonal superposition of the two decaying vectors produces a solution whose norm (length) increases before it eventually decays to zero. During this process, the solution progressively aligns itself along the least stable direction. On the left of the figure, the normal case is displayed; the initial condition (again, thick blue line) is represented as a superposition of two orthogonal vectors. Their initial length is however on the same order as the length of the initial condition. As before, we assume a more rapid decay along one vector (in green) than along the other (in red). No stretching of the vector, but rather a monotonic decay, is observed.

Nonorthogonality of the eigenvectors thus enabled the short-time amplification of initial energy, even though—based on eigenvalues alone—the system is asymptotically stable. The reason for the nonorthogonality of the eigenvectors lies in the non-normality of the system matrix A. Formally, a non-normal matrix (or operator) does not commute with its adjoint, which is mathematically expressed as $\mathsf{A}\mathsf{A}^+ \neq \mathsf{A}^+\mathsf{A}$ with $^+$ denoting the adjoint.[63]

From the simple example above, we conclude that for non-normal LTI-systems of the form (1) eigenvalues become an asymptotic tool describing the long-term behavior. The short-term behavior cannot be described by eigenvalues alone; instead the angle between the eigenvectors plays an important role in explaining and quantifying transient growth of energy (or of other state-vector norms).

If eigenvalues describe the long-term behavior ($t \to \infty$) for non-normal systems, we are interested in other sets in the complex plane that describes the short-time dynamics. One of these sets is given by the numerical range of the matrix A and can be easily derived by reconsidering the expression for the energy growth rate $\gamma(t)$. We have[63]

$$\begin{aligned}\gamma(t) &= \frac{1}{\|\mathbf{q}\|^2}\frac{d}{dt}\langle \mathbf{q}, \mathbf{q}\rangle = \frac{1}{\|\mathbf{q}\|^2}\left\langle \frac{d}{dt}\mathbf{q}, \mathbf{q}\right\rangle + \frac{1}{\|\mathbf{q}\|^2}\left\langle \mathbf{q}, \frac{d}{dt}\mathbf{q}\right\rangle \\ &= 2\ \mathrm{Real}\left(\frac{\langle \mathsf{A}\mathbf{q}, \mathbf{q}\rangle}{\langle \mathbf{q}, \mathbf{q}\rangle}\right).\end{aligned} \tag{5}$$

The last expression establishes a link between the energy growth rate γ and the set of all Rayleigh quotients $\langle \mathsf{A}\mathbf{q}, \mathbf{q}\rangle / \langle \mathbf{q}, \mathbf{q}\rangle$ of our matrix A; this set is known as the numerical range of A. It is easy to show that the numerical range of A is a convex set in the complex plane that contains the spectrum of A (the Rayleigh quotient becomes an eigenvalue of A if $\mathbf{q}$ is chosen as an eigenvector). Less obvious is the fact that the numerical range degenerates into the convex hull of the spectrum of A, if A is normal.[65] For our case (and a Reynolds number of $Re = 10$), the numerical range is plotted in the complex plane, together with the spectrum of A (Figure 4(a)).

We verify that for non-normal matrices A the numerical range is convex and contains the spectrum (the eigenvalues, illustrated by the two black symbols). What is more important, however, is that the numerical range reaches into the unstable half-plane, shaded in gray. According to equation (5) this means that there exist positive energy growth rates, despite the fact that both eigenvalues are confined to the stable half-plane. Setting the off-diagonal term in A to zero yields a diagonal—and thus normal—matrix. The numerical range in this case is given by the convex hull of the spectrum; this is displayed in Figure 4(b). Rayleigh quotients fall on a line that connects the two eigenvalues; consequently, the energy growth rates will remain negative for all times. This is consistent with our earlier findings.

It is interesting and instructive to determine the *initial* energy growth rate, that is, the energy growth rate at $t = 0^+$. For this, we use a Taylor series expansion of

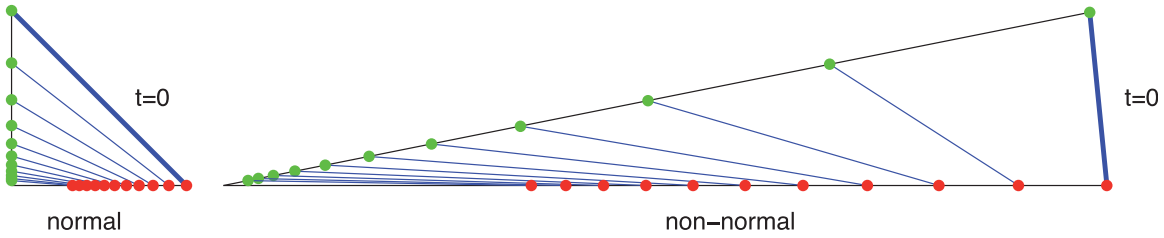


Figure 3. Geometric sketch of energy growth/decay in a two-dimensional orthogonal (left) and nonorthogonal (right) system. In either case, the two vector components contract, ultimately yielding a solution vector of zero length. In the normal case, monotonic decay toward a zero-length solution is observed; in the non-normal case, transient growth prevails before the asymptotic limit of a zero-length vector is reached.

the matrix exponential for small times, that is, $\exp(t\mathsf{A}) \approx I + t\mathsf{A}$, to arrive at

$$\gamma(0^+) = \lim_{t\to 0^+} \frac{1}{\|\mathbf{q}_0\|^2}\frac{d}{dt}\langle \mathbf{q},\mathbf{q}\rangle = \lim_{t\to 0^+} \frac{1}{\|\mathbf{q}_0\|^2} \frac{d}{dt}\langle (I+t\mathsf{A})\mathbf{q}_0,(I+t\mathsf{A})\mathbf{q}_0\rangle = \frac{\langle \mathbf{q}_0,(\mathsf{A}+\mathsf{A}^+)\,\mathbf{q}_0\rangle}{\langle \mathbf{q}_0,\mathbf{q}_0\rangle}. \tag{6}$$

The final expression represents a Rayleigh quotient for a normal matrix, $\mathsf{A}+\mathsf{A}^+$, which attains its maximum at $\lambda_{\max}(\mathsf{A}+\mathsf{A}^+)$. This means that the largest eigenvalue of the matrix $\mathsf{A}+\mathsf{A}^+$, also known as the numerical abscissa of A, gives the largest initial energy growth rate of our system.[32,63]

After establishing that for non-normal systems eigenvalues quantify the dynamic behavior for large times ($t\to\infty$), while the numerical range gives information about the short time behavior ($t=0^+$), a third quantity in the complex plane describes the behavior at intermediate times—though only approximately. For asymptotically stable systems the peak $G_{\max}$ of the matrix exponential (see the blue and black curve in Figure 2(a)) can be bounded by

$$\max_{\mathrm{Real}(z)>0} \mathrm{Real}(z)\|(z\mathrm{I}-\mathsf{A})^{-1}\| \le \sqrt{G_{\max}} \le \frac{1}{2\pi}\oint_C \|(z\mathrm{I}-\mathsf{A})^{-1}\|\,\mathrm{d}\,|z|. \tag{7}$$

The lower bound is based on a Laplace transform of the matrix exponential, while the upper bound stems from an application of Cauchy's integral formula (along a contour C that encloses the spectrum of A); details of these bounds are given elsewhere.[63,66] It is interesting to note, however, that both bounds involve the quantity $(z\mathrm{I}-\mathsf{A})^{-1}$ which is referred to as the resolvent and is defined in the complex plane ($z\in\mathbb{C}$), with pole singularities where z coincides with an eigenvalue of A. It seems appropriate then to consider the norm of the resolvent in the complex plane. This has been done in Figure 4 where contour lines of constant resolvent norm have been added in gray. For the normal case (Figure 4(b)) the resolvent contours degenerate to concentric circles around the two eigenvalues, with the contour levels dropping inversely proportional to the distance to the closest eigenvalue. For the non-normal case (Figure 4(a)) the contours of the resolvent norm show values that exceed the inverse distance to the closest eigenvalue. We conclude from equation (7) and from Figure 4 that the resolvent value away from the eigenvalues plays a significant role. In other words, one should not only concentrate on the singularities of the resolvent (the eigenvalues), regions of the complex plane where the resolvent is not infinite but nevertheless large (compared to the one-over-distance behavior) are equally important.[32,64,66,67]

In summary, non-normal systems with their non-orthogonal eigenvectors exhibit a rich dynamical behavior which requires more complex tools to describe and quantify. For short times, the numerical range determines the initial energy growth rate; for intermediate times, expressions based on the resolvent can be used to approximate the maximum transient growth; and only for asymptotically large times do the eigenvalues describe the system's behavior. For normal systems, these three tools collapse into one: the numerical range is the convex hull of the spectrum, and the resolvent is given by a one-over-distance function to the spectrum; both quantities carry no more information than the eigenvalues themselves. The eigenvalues are thus the only quantity one has to consider; for normal systems they describe the dynamic behavior for *all* times.

For non-normal systems that exhibit substantial transient growth, it is often interesting to determine the specific initial condition that achieves the maximum energy amplification $G_{\max}$ or the maximum energy amplication at a prescribed time. By its definition (3), the norm of the matrix exponential $G(t) = \|\exp(t\mathsf{A})\|^2$ contains an optimization over all initial conditions, and

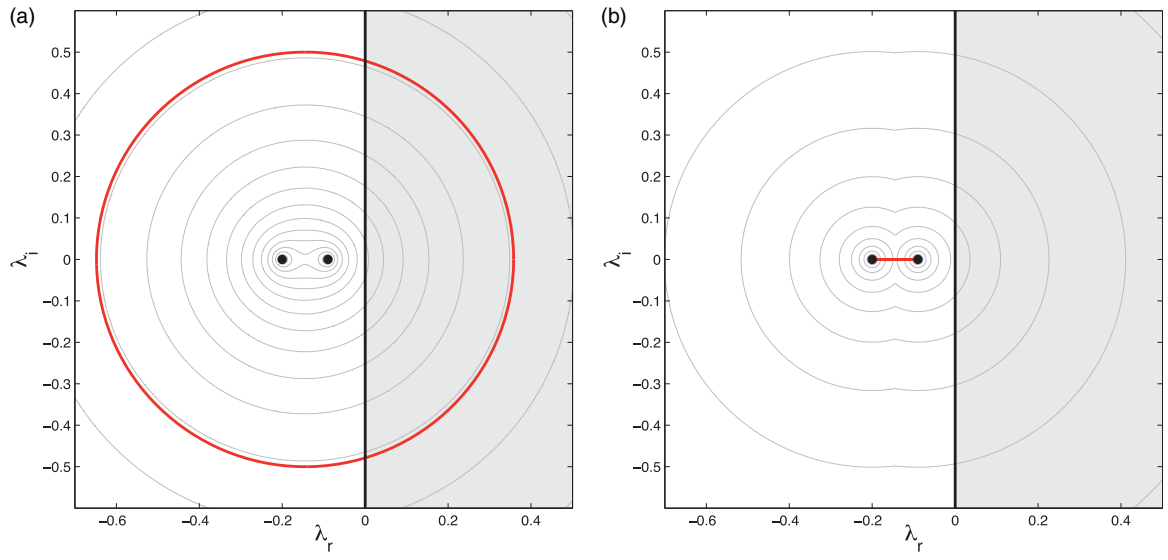


Figure 4. (a) Boundary of the numerical range (in red) and spectrum (in black symbols) of the non-normal matrix A for $Re = 10$. (b) Boundary of the numerical range (in red) and spectrum (in black symbols) of A when the off-diagonal term is set to zero, thus rendering A a normal matrix.

the curves in Figure 2 thus represent envelopes over many individual realizations; each point on these optimal curves may have been generated by a different initial condition. To recover the specific initial condition that produces optimal energy amplification at a given time τ we write

$$\exp(\tau A)\mathbf{q}_0 = \|\exp(\tau A)\|\mathbf{q}_\tau \tag{8}$$

which states that the unit-norm initial condition $\mathbf{q}_0$ is propagated over a time span τ by $\exp(\tau A)$ resulting in another unit-norm state vector $\mathbf{q}_\tau$ that is multiplied by the amplification factor $\|\exp(\tau A)\|$. Expression (8) is reminiscent of a singular value decomposition (SVD), namely $CV = U\Sigma$ with V and U as unitary matrices with orthonormalized columns and Σ as a diagonal matrix. Recalling that σ_1 (the dominant singular value) is $\|C\|$, the principal component of the SVD reads $Cv_1 = u_1\|B\|$ where v_1 and u_1 denote the first column of V and U. Comparing this last expression with (8) we identify $\mathbf{q}_0$ as first column of the right singular vectors and $\mathbf{q}_\tau$ as the first column of the left singular vectors of $\exp(\tau A)$. The computational procedure to determine the optimal initial condition for a prescribed time τ consists of a SVD of the propagator $\exp(\tau A)$ from which the optimal initial condition $\mathbf{q}_0$ follows as the principal right singular vector, the optimal output $\mathbf{q}_\tau$ is given by the principal left singular vector.[32,64] An elaborate discussion of SVD in the context of a thermoacoustic system is given in Kedia et al.[68]

Extensions and further results of nonmodal analysis. The de-emphasis of eigenvalues for describing the dynamic behavior of non-normal systems translates to many other areas where eigenvalues have traditionally prevailed. One area with important applications in fluid mechanics is receptivity analysis which is, for example, concerned with the response of a boundary layer to external disturbances or to wall roughness. The governing equations for receptivity constitute a driven system, and the maximum response in energy to a unit-energy forcing is often taken as a receptivity measure. Traditionally, this measure is linked to a resonance argument. However, resonances are commonly described by the closeness of the driving frequency to the eigenvalues of the driven system. For normal systems, this is a necessary and sufficient condition for a large response; for non-normal systems, this eigenvalue-based analysis is inadequate. In general, the maximum response of a driven system is given by the resolvent norm. As we have seen above, a large resolvent norm is not necessarily associated with closeness to an eigenvalue, when the system is non-normal. In this case, large responses can also be generated for driving frequencies that are far from any eigen-frequency of the system. A resonance of this type is often referred to as a pseudo-resonance.[61] These concepts are becoming increasingly important in receptivity analysis, but also in flow control and model reduction efforts.

The existence of transient amplification of energy at subcritical parameter values raises the question whether this amplification is sufficient to trigger nonlinear effects.[69–71] To investigate this question, we will study

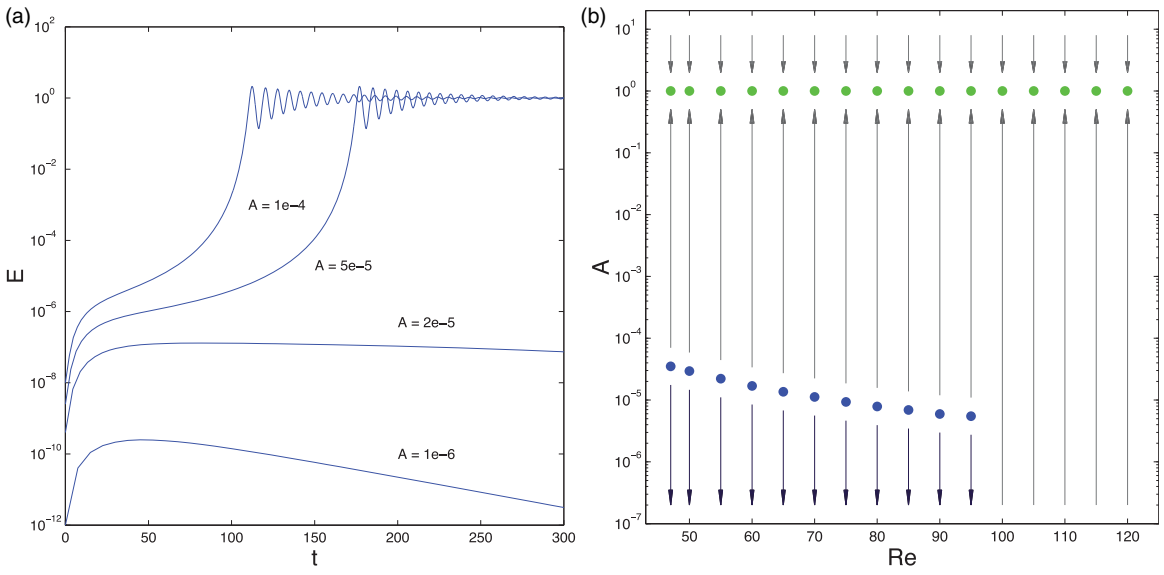


Figure 5. (a) Perturbation energy versus time for the nonlinear system (equation (9)) starting with $\mathbf{q}_0 = A(0, 1)^T$ and four different amplitudes A. (b) Bifurcation diagram for the nonlinear system (equation (9)), indicating the triggering amplitudes (blue symbols) and the nonlinear steady state (green symbols). The critical Reynolds number is $Re_{crit} = 100$.

the nonlinear system

$$\frac{d}{dt}\begin{pmatrix} q_1 \\ q_2 \end{pmatrix} = \begin{pmatrix} \frac{1}{100} - \frac{1}{Re} & 1 \\ 0 & -\frac{2}{Re} \end{pmatrix}\begin{pmatrix} q_1 \\ q_2 \end{pmatrix} + \sqrt{q_1^2 + q_2^2}\underbrace{\begin{pmatrix} 0 & -1 \\ 1 & 0 \end{pmatrix}}_{B}\begin{pmatrix} q_1 \\ q_2 \end{pmatrix} \tag{9}$$

which has the same linear operator as before. The nonlinear terms have been chosen to preserve energy, that is, $\mathbf{q}^H B\mathbf{q} = 0$, thus mimicking the nonlinear terms of the incompressible Navier–Stokes equations. Figure 5(a) displays simulations for $Re = 50$ starting with the initial condition $\mathbf{q}_0 = A(0, 1)^T$ of increasing amplitude A. For sufficiently small initial amplitude A we observe the familiar scenario of short-term transient growth followed by an asymptotic decay. As the initial amplitude surpasses a critical value A_{crit} nonlinear effects will pull the phase curves toward a non-zero steady state. In Figure 5(a), we see a rapid increase in energy and an oscillatory settling into a flow state with $E = 1$. For still higher initial amplitudes this unit-energy flow state is reached more quickly. It is important to realize that the nonlinear term cannot produce energy by itself; it simply redistributes energy from decaying directions in phase-space to transiently growing ones, thus harvesting the full potential for transient growth by a nonlinear feedback mechanism. This mechanism is often referred to as bootstrapping.[61]

The question then arises about the critical initial amplitudes A_{crit} that delineate attraction to the nonlinear unit-energy state from decay toward the zero-energy solution. These triggering amplitudes are part of a bifurcation diagram and, in general, are very difficult to determine since they involve an optimization of a nonlinear system over all admissable initial conditions. For our case of a 2×2, the optimization can be accomplished rather straightforwardly. The results are given in Figure 5(b); it presents the critical amplitudes (optimized over all initial conditions) versus the Reynolds number (as blue symbols). For initial amplitudes above this line, we can approach the nonlinear steady state (indicated by green symbols); for amplitudes below this line, we decay toward the "laminar" state. The critical amplitude becomes zero for $Re > 100$ since a linear modal instability will amplify even infinitesimal perturbations until the nonlinear ($E = 1$)-state is reached.

A bifurcation like the one depicted in Figure 5(b) is known as a subcritical bifurcation. In this case, finite-amplitude states become unstable *before* the infinitesimal state does. As a consequence, over a finite range of Reynolds numbers two stable states coexist: the stable infinitesimal state (which is reached, if the initial amplitude is less than the critical one) and the stable finite-amplitude state (which can be reached, if the initial amplitude exceeds the critical one). In contrast, a bifurcation is labelled supercritical if finite-amplitude states become unstable *after* the infinitesimal state has become unstable. Fluid mechanics knows a wide range of phenomena and configurations that fall either into the subcritical (e.g., wall-bounded shear flows) or the supercritical (e.g., Rayleigh–Bénard convection) category.

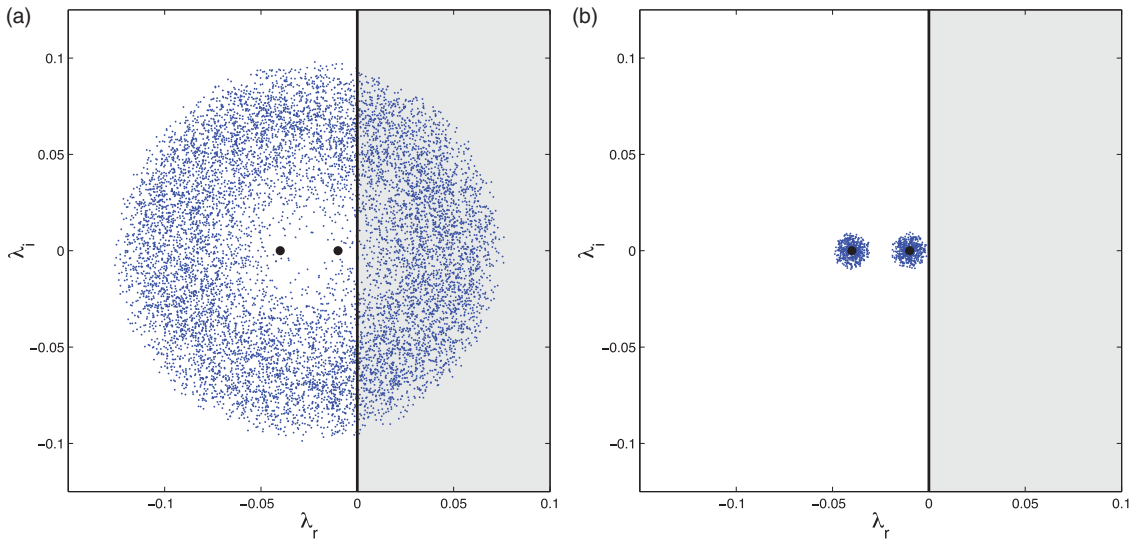


Figure 6. Sensitivity of eigenvalues for (a) the non-normal system at $Re = 50$, and (b) the normal system (with zero off-diagonal term) at the same Reynolds number. In both cases, the matrix A has been perturbed by random matrices of norm 10^{-2}.

For nonlinearities that preserve the energy norm, as is the case for our 2×2 system and is the case for the incompressible Navier–Stokes equations, there is an interesting link between the bifurcation behavior (supercritical/subcritical) and the non-normality of the linear operator. A non-normal linear operator is necessary for a subcritical bifurcation behavior, since—in the absence of energy production by nonlinear terms—only a linear operator will provide the required energy amplification to reach the nonlinear steady state. This linear energy amplification mechanism has to be active even before modal (eigenvalue) instabilities are present; only a non-normal operator can accomplish this. In other words and in reference to Figure 4(a), the numerical range has to cross into the unstable half-plane before the eigenvalues do. This can only be true of a non-normal operator, where the numerical range is detached from the spectrum. On the contrary, a normal linear operator can only cause a supercritical bifurcation behavior. In this case, energy growth and modal growth toward a finite-amplitude steady-state occur at the same parameter value (in our case, the Reynolds number), since the numerical range is attached to the least stable mode; both, the numerical range and the least stable mode cross into the unstable half-plane at the same critical parameter. It is important to stress that non-normality is a necessary condition for subcritical behavior and that normality is a sufficient condition for supercritical behavior; in addition, the above arguments only hold when nonlinearities preserve energy. In the case of thermoacoustic systems studies so far indicate that nonlinearities are not energy conserving.

Non-normal linear systems play an important role in many physical processes. The above tools (matrix exponential, resolvent, numerical range, etc.) give a means to isolate and quantify effects due the non-normality of the underlying linear system. The first indication of non-normality that is often encountered in numerical experiments is a marked sensitivity of eigenvalues to minute perturbations. In Figure 6 we perturb the system matrix A by a random matrix E of norm 10^{-2} and display the eigenvalues of $\mathsf{A} + E$ for multiple realizations.[63,64,67] For the non-normal case (Figure 6(a)), we observe that a small perturbation displaces the eigenvalues by a disproportionately large amount, yielding eigenvalues even far in the unstable domain. The same amount of perturbations has little effect on the eigenvalues for the normal matrix (Figure 6(b)): the displacement of the eigenvalue is bounded by the size of the perturbation. A connection can be made between the maximum displacement of eigenvalues and the resolvent norm contour associated with the inverse perturbation norm $\|E\|^{-1}$.

A more general framework. The analysis of non-normal systems can be generalized to more complex systems, beyond simple LTI-systems, by casting it in a variational framework and by performing the optimization explicitly, rather than by invoking it via the definition of an induced matrix norm (as in equation (3)). The variational formulation allows substantially greater flexibility in treating fluid problems that do not strictly fall within the constraints above.[72]

We are still interested in the maximum energy growth over a given time span $[0\ \tau]$ optimized over all

admissible initial conditions; however, rather than making use of the fundamental solution of our linear system (as before, by substituting the matrix exponential in (3)), we instead impose the governing equation as a constraint via a Lagrangian multiplier $\mathbf{p}$. This Lagrangian multiplier is also referred to as the adjoint variable. We get the optimization problem

$$\mathcal{J} = \frac{\|\mathbf{q}(\tau)\|}{\|\mathbf{q}_0\|} - \left\langle \mathbf{p}, \frac{d}{dt}\mathbf{q} - \mathsf{A}\mathbf{q} \right\rangle \quad \rightarrow \quad \max. \tag{10}$$

It is evident that this approach is more general: the governing equations are always known, whereas an explicit solution is only given under exceptional circumstances and/or can be obtained only at substantial numerical cost. The above functional $\mathcal{J}$ is to be maximized with respect to all independent variables: $\mathbf{q}, \mathbf{q}_0$ and $\mathbf{p}$. First variations with respect to these three variables yield three respective equations

$$\frac{d}{dt}\mathbf{q} = \mathsf{A}\mathbf{q}, \tag{11}$$

$$-\frac{d}{dt}\mathbf{p} = \mathsf{A}^{+}\mathbf{p}, \tag{12}$$

$$\mathbf{q}_0 = \frac{E_0}{E_\tau}\mathbf{p}(0), \tag{13}$$

with $E_0 = \langle \mathbf{q}_0, \mathbf{q}_0 \rangle$ and $E_\tau = \langle \mathbf{q}(\tau), \mathbf{q}(\tau) \rangle$. The first two equations are evolution equations for the direct variable $\mathbf{q}$ and the adjoint variable $\mathbf{p}$, respectively. The third equation (from the first variation of $\mathcal{J}$ with respect to the initial condition $\mathbf{q}_0$) provides a link between the direct and adjoint variables. The above three equations can be set up as an iterative optimization scheme sketched in Figure 7.[73–76] Starting with an initial guess, we solve the direct equation (11) over the prescribed interval $[0, \tau]$. The final solution is then propagated backwards in time from $t = \tau$ to $t = 0$ using the adjoint equation (12). The solution of the adjoint equation is then used in equation (13) to update the initial condition $\mathbf{q}_0$ for the next iteration. The direct-adjoint cycle is repeated until convergence is reached.

The variational framework is not restricted to enforce only linear evolution equations, it can easily be applied to compute optimal initial conditions that maximize transient energy growth when propagated by a nonlinear equation. In this case, we write

$$\mathcal{J} = \frac{\|\mathbf{q}(\tau)\|}{\|\mathbf{q}_0\|} - \left\langle \mathbf{p}, \frac{d}{dt}\mathbf{q} - \mathbf{f}(\mathbf{q}) \right\rangle \quad \rightarrow \quad \max. \tag{14}$$

The derivation of the iterative scheme proceeds along the same line. After taking the first variation with respect to the three variables, we recover the nonlinear evolution equation for $\mathbf{q}$, obtain a linear evolution equation for the adjoint variable $\mathbf{p}$ and get an expression linking $\mathbf{q}$ and $\mathbf{p}$. Even though the adjoint equation is linear in $\mathbf{p}$, its coefficients depend on the direct variables $\mathbf{q}$. This fact complicates the iterative optimization scheme, since during the solution of the direct equation snapshots of $\mathbf{q}$ need to stored; these snapshots are then used (in time-reversed order) to evaluate the coefficients for the backward-integration of the adjoint equation (Figure 8).[33,77–79] For small-scale problems (e.g., our 2×2 model problem), the storage of all produced fields does not pose a problem, but for large-scale applications with many degrees of freedom, memory issues become relevant, and specific storage strategies have to be employed. Flow fields at prescribed instants in time (known as checkpoints) are stored and the coefficients for the backward integration have to be reconstituted from these checkpoint fields.[80] This involves short forward-integrations of the direct system using the stored checkpoint solutions as initial conditions. An optimal placement of checkpoints, given a total amount of available storage, leads to a non-equidistant spacing in time (not shown in Figure 8).

Application to fluid systems. Over the past decades transient growth and nonmodal analysis have become

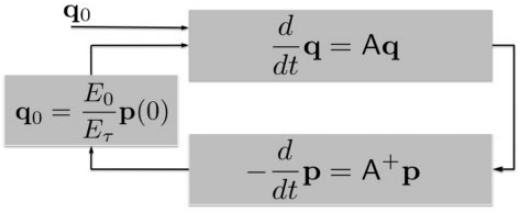


Figure 7. Sketch of iterative optimization scheme based on the direct and adjoint governing equations, derived from a variational framework.

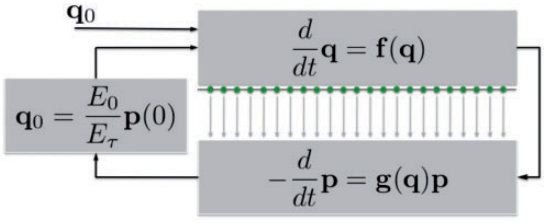


Figure 8. Sketch of iterative optimization scheme based on the nonlinear, direct and variable-coefficient, adjoint governing equations, derived from a variational framework. The checkpoints at which the direct solutions are stored are indicated by green symbols.

important and accepted tools of fluid dynamics.[32] In numerous studies, the presence of non-normal linear operators and its consequence on the dynamic processes have been recognized.

In bypass transition, defined as a route to turbulence that does not rely on an exponential instability, the importance of linear growth mechanisms that operate efficiently at subcritical conditions has been acknowledged.[81] These mechanisms favor structures in the flow that markedly deviate from modal ones; in particular, streaks, that is, fluid elements elongated in the streamwise direction, have been found as the omnipresent manifestation of nonmodal dynamics. Both numerical simulations and experiments have confirmed their importance.

The same elongated structures also play an important role in receptivity studies, where perturbations in the freestream trigger disturbance growth in the boundary layer. In this case, nonmodal processes compete with modal ones.[82]

In fully developed turbulent flow, the importance of a linear mechanism based on non-normality has been recognized.[83,84] In this case, it is part of a self-sustaining process that involves transient energy amplification, secondary breakdown, and nonlinear regeneration. Even though the entire cycle is nonlinear, without a linear non-normal component it would collapse, yielding relaminarized flow.[85]

Much has been gained in stability theory and fluid dynamics by abandoning the concept of Lyapunov (time-asymptotic) stability in favor of a more general, finite-time stability notion. Most fluid devices or configurations have an instrinsic time-scale that is often far shorter than the asymptotic limit required for Lyapunov stability. Moreover, exponential growth rates are often too weak to account for significant energy growth over short or intermediate time intervals. For this reason, it seems fitting to introduce a characteristic time-scale into the definition of stability and adopt mathematical tools that describe fluid processes on a finite rather than infinite time horizon. Some of these tools have been introduced above. Over the years, these concepts have provided deeper insight into many fluid dynamical mechanisms; the same is expected for thermoacoustic systems.

A toy model for the Rijke tube

A horizontal Rijke tube with an electric heat source is a convenient system for studying the fundamental principles of thermoacoustic instability both experimentally and theoretically (Figure 9). The mean flow is imposed by a fan, rather than by natural convection, so the heater power and the mean flow are controlled independently. We present here a simple model for the horizontal Rijke tube, which has been used by

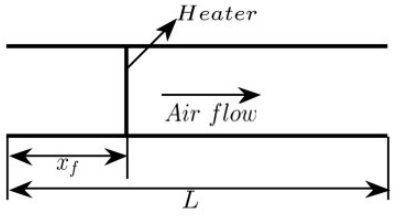


Figure 9. Diagram of a horizontal Rijke tube.

Refs.[21,22,24,25,33,36,38,86] A more elaborate model for the Rijke tube can be found in Mariappan and Sujith.[38]

Governing equations

The tube has length L_0 and a hot wire is placed distance $\tilde{x}_f$ from one end. A base flow is imposed with velocity u_0. The physical properties of the gas in the tube are described by c_v, γ, R, and λ, which represent the constant volume specific heat capacity, the ratio of specific heats, the gas constant, and the thermal conductivity, respectively. The unperturbed quantities of the base flow are ρ_0, p_0, and T_0, which represent density, pressure, and temperature, respectively. From these one can derive the speed of sound $c_0 \equiv \sqrt{\gamma R T_0}$ and the Mach number of the flow $M \equiv u_0/c_0$.

Acoustic perturbations are considered on top of this base flow. In dimensional form, the perturbation velocity and perturbation pressure are represented by the variables $\tilde{u}$ and $\tilde{p}$, respectively and distance and time are represented by the coordinates $\tilde{x}$ and $\tilde{t}$, respectively. Quantities evaluated at the hot wire's position, $\tilde{x}_f$, have subscript f. At the hot wire, the rate of heat transfer to the gas is given by $\dot{Q}$. This heat transfer is applied at the wire's position by multiplying $\tilde{\dot{Q}}$ by the dimensional Dirac delta distribution $\tilde{\delta}_D(\tilde{x} - \tilde{x}_f)$. Acoustic damping, which will be described in §4.4, is represented by ζ.

The dimensional governing equations for the perturbation are the momentum equation and the energy equation

$$\tilde{F}_1 \equiv \rho_0 \frac{\partial \tilde{u}}{\partial \tilde{t}} + \frac{\partial \tilde{p}}{\partial \tilde{x}} = 0, \tag{15}$$

$$\tilde{F}_2 \equiv \frac{\partial \tilde{p}}{\partial \tilde{t}} + \gamma p_0 \frac{\partial \tilde{u}}{\partial \tilde{x}} + \zeta \frac{c_0}{L_0} \tilde{p} - (\gamma - 1)\tilde{\dot{Q}}\tilde{\delta}_D(\tilde{x} - \tilde{x}_f) = 0. \tag{16}$$

The heat release is modelled with a form of King's law adapted from Heckl,[22] in which the heat release increases with the square root of the velocity. Surface heat transfer and subsequent thermal diffusion between the wire and the fluid are modelled by a constant time

delay, $\tilde{\tau}$, between the time when the velocity acts and the time when the corresponding heat release is felt by the perturbation

$$\tilde{\dot{Q}} = \frac{2L_w(T_w - T_0)}{S\sqrt{3}}\left(\pi\lambda c_v\rho_0\frac{d_w}{2}\right)^{\frac{1}{2}} \times \left(\left|\frac{u_0}{3} + \tilde{u}_f(\tilde{t} - \tilde{\tau})\right|^{\frac{1}{2}} - \left(\frac{u_0}{3}\right)^{\frac{1}{2}}\right), \tag{17}$$

where L_w, d_w, and T_w represent the length, diameter, and temperature of the wire, respectively and S represents the cross-sectional area of the tube. Heckl[22] based the off-set of $u_0/3$ on experimental results. It is now apparent that recent papers have gone beyond the range of validity of the model, specifically when $u < -u_0/3$, and that this caused oscillations to saturate earlier than they should have done. The results are qualitatively correct, however, and we have decided to retain Heckl's law here so that this article is consistent with previous articles.

The nondimensional governing equations

Reference scales for speed, pressure, length, and time are taken to be u_0, $p_0\gamma M$, L_0, and L_0/c_0, respectively. The dimensional variables, coordinates, and Dirac delta can then be written as

$$\tilde{u} = u_0 u, \quad \tilde{p} = p_0\gamma M p, \quad \tilde{x} = L x \tilde{t} = (L/c_0)t, \quad \tilde{\delta_D}(\tilde{x} - \tilde{x}_f) = \delta_D(x - x_f)/L, \tag{18}$$

where the quantities without a tilde or subscript 0 are dimensionless.

A remark on nondimensionalizing the acoustic velocity using the mean flow velocity is called for here. It has been shown that for systems that work at very low Mach number, the convective terms in the wave equation can be neglected.[87] However, this thermoacoustic system is driven by a heat release rate which has a dependence on the mean convective velocity. Hence, we choose the include the convective velocity in the scaling law for acoustic velocity. Further, it is known when limit cycle is attained, the amplitude of the acoustic velocity is of the order of the mean convective velocity. Scaling the acoustic velocity using the mean flow velocity leads to a nondimensional acoustic velocity amplitude of 1, when the acoustic velocity equals the mean flow velocity.

Substituting equation (18) into the dimensional governing equations (15) and (16) and making use of the definition of c_0 and the ideal gas law, $p_0 = \rho_0 R T_0$, gives the dimensionless governing equations

$$F_1 \equiv \frac{\partial u}{\partial t} + \frac{\partial p}{\partial x} = 0, \tag{19}$$

$$F_2 \equiv \frac{\partial p}{\partial t} + \frac{\partial u}{\partial x} + \zeta p - \beta\left(\left|\frac{1}{3} + u_f(t - \tau)\right|^{\frac{1}{2}} - \left(\frac{1}{3}\right)^{\frac{1}{2}}\right)\delta_D(x - x_f) = 0, \tag{20}$$

where

$$\beta \equiv \frac{1}{p_0\sqrt{u_0}}\frac{(\gamma - 1)}{\gamma}\frac{2L_w(T_w - T_0)}{S\sqrt{3}}\left(\pi\lambda c_v\rho_0\frac{d_w}{2}\right)^{\frac{1}{2}} \tag{21}$$

The system has four control parameters: ζ, which is the damping; β, which encapsulates all relevant information about the hot wire, base velocity and ambient conditions; τ, which is the time delay, and x_f, which is the position of the wire.

The boundary conditions and the discretized governing equations

When appropriate boundary conditions in x are set, the governing equations (19) and (20) reduce to an initial value problem in t. For the system examined in this article, $\partial u/\partial x$ and p are both set to zero at the ends of the tube. These boundary conditions are enforced by choosing basis sets that match these boundary conditions

$$u(x, t) = \sum_{j=1}^{N}\eta_j(t)\cos(j\pi x), \tag{22}$$

$$p(x, t) = -\sum_{j=1}^{N}\left(\frac{\dot{\eta}_j(t)}{j\pi}\right)\sin(j\pi x), \tag{23}$$

where the relationship between η_j and $\dot{\eta}_j$ has not yet been specified. In this discretization, all the basis vectors are orthogonal.

The state of the system is given by the amplitudes of the modes that represent velocity, η_j, and those that represent pressure, $\dot{\eta}_j/j\pi$. These are given the notation $\mathbf{u} \equiv (\eta_1, \ldots, \eta_N)^T$ and $\mathbf{p} \equiv (\dot{\eta}_1/\pi, \ldots, \dot{\eta}_N/N\pi)^T$. The state vector of the discretized system is the column vector $\mathbf{x} \equiv (\mathbf{u}; \mathbf{p})$.

The governing equations are discretized by substituting equations (22) and (23) into equations (19) and (20). As described in §4.4, the damping, ζ, is dealt with by assigning a damping parameter, ζ_j, to each mode. Equation (20) is then multiplied by $\sin(k\pi x)$ and

integrated over the domain $x = [0, 1]$. The governing equations then reduce to two delay differential equations (DDEs) for each mode, j

$$F_{1G} \equiv \frac{\mathrm{d}}{\mathrm{d}t}\eta_j - j\pi\left(\frac{\dot{\eta}_j}{j\pi}\right) = 0, \tag{24}$$

$$F_{2G} \equiv \frac{\mathrm{d}}{\mathrm{d}t}\left(\frac{\dot{\eta}_j}{j\pi}\right) + j\pi\eta_j + \zeta_j\left(\frac{\dot{\eta}_j}{j\pi}\right)\cdots + \cdots + 2\beta\left(\left|\frac{1}{3} + u_f(t-\tau)\right|^{\frac{1}{2}} - \left(\frac{1}{3}\right)^{\frac{1}{2}}\right)\sin(j\pi x_f) = 0, \tag{25}$$

where

$$u_f(t-\tau) = \sum_{k=1}^{N}\eta_k(t-\tau)\cos(k\pi x_f). \tag{26}$$

Decomposition into a set of coupled oscillator equations (24)–(25) is a standard technique in thermoacoustics and is described in several early papers, such as Culick.[88] Section 4.3–4.4 of Culick[2] contains a discussion of this method, called spatial averaging, and the closely related Galerkin method, which give the same result for the system in this article.

Damping

For the system examined in this article, p and $\partial u/\partial x$ are both set to zero at the ends of the tube, which means that the system cannot dissipate acoustic energy by doing work on the surroundings. Furthermore, the acoustic waves are planar, which means that the system cannot dissipate acoustic energy in the viscous and thermal boundary layers at the tube walls. Both types of dissipation are modelled by the damping parameter for each mode

$$\zeta_j = c_1 j^2 + c_2 j^{1/2}, \tag{27}$$

where c_1 and c_2 are the same for each mode. This model was used in Balasubramanian and Sujith[36] and Kedia et al.[68] and was based on correlations developed by Matveev[21] from models in Landau and Lifshitz.[89]

The definition of the acoustic energy norm

For the optimization procedure, it is necessary to define some measure of the size of the perturbations. Several measures are possible and each could give a different optimal. The most convenient measure is the acoustic energy per unit volume, $\tilde{E}$, because it is easy to calculate and has a simple physical interpretation.[68]

The acoustic energy per unit volume, $\tilde{E}$ consists of a kinetic component, $\widetilde{E_k}$ and a pressure potential component, $\widetilde{E_p}$. In dimensional form it is given by

$$\tilde{E} = \widetilde{E_k} + \widetilde{E_p} = \frac{1}{2}\rho_0\left(\tilde{u}^2 + \frac{\tilde{p}^2}{\rho_0^2 c_0^2}\right). \tag{28}$$

Substituting for $\tilde{u}$ and $\tilde{p}$ from equation (18), making use of the ideal gas relation and defining the reference scale for energy per unit volume to be $\rho_0 u_0^2$, the dimensionless acoustic energy per unit volume, E, is given by Kedia et al.[68]

$$\begin{aligned} E &= \frac{1}{2}u^2 + \frac{1}{2}p^2 = \frac{1}{2}\sum_{j=1}^{N}\eta_j^2 + \frac{1}{2}\sum_{j=1}^{N}\left(\frac{\dot{\eta}_j}{j\pi}\right)^2 \\ &= \frac{1}{2}\mathbf{x}^H\mathbf{x} = \frac{1}{2}\|\mathbf{x}\|^2, \end{aligned} \tag{29}$$

where $\|\cdot\|$ represents the 2-norm. The rate of change of the acoustic energy with time is

$$\frac{\mathrm{d}E}{\mathrm{d}t} = u\frac{\mathrm{d}u}{\mathrm{d}t} + p\frac{\mathrm{d}p}{\mathrm{d}t} = \sum_{j=1}^{N}\eta_j\frac{\mathrm{d}\eta_j}{\mathrm{d}t} + \sum_{j=1}^{N}\left(\frac{\dot{\eta}_j}{j\pi}\right)\frac{\mathrm{d}}{\mathrm{d}t}\left(\frac{\dot{\eta}_j}{j\pi}\right) \tag{30}$$

$$= -\sum_{j=1}^{N}\zeta_j\left(\frac{\dot{\eta}_j}{j\pi}\right)^2 - \sum_{j=1}^{N}2\beta\left(\frac{\dot{\eta}_j}{j\pi}\right) \times \left(\left|\frac{1}{3} + u_f(t-\tau)\right|^{\frac{1}{2}} - \left(\frac{1}{3}\right)^{\frac{1}{2}}\right)\sin(j\pi x_f). \tag{31}$$

The first term on the right hand side of equation (31) represents damping and is always negative. The second term is the instantaneous value of $p\dot{Q}$ and is the rate at which thermal energy is transferred to acoustic energy at the wire. It is worth noting that this transfer of energy can be in either direction.

In general, care should be taken in adopting the appropriate norm. A number of definitions of disturbance energies are available; for a recent review, see George and Sujith.[90] Chu's norm[91] was used in Mariappan and Sujith[42] and Wieczoerk et al.,[45] whereas Mariappan et al.[37] used Myers' energy.[92] The consequences of choosing an inappropriate norm are highlighted in Wieczoerk et al.[45]

The linearized governing equations

Non-normality, which is central to this article, is a linear phenomenon. It is most easily examined when the governing equations are linearized around $\mathbf{x} = 0$ and expressed in the form $\mathrm{d}\mathbf{x}/\mathrm{d}t = \mathbf{L}\mathbf{x}$, where $\mathbf{x}$ represents the state of the system and $\mathbf{L}$ represents the

evolution operator or matrix. Two linearizations are required in order to express the governing equations in this form. The first linearization, which is valid for $u_f(t-\tau) \ll 1/3$, is performed on the square root term in equations (20) and (25)

$$\left(\left|\frac{1}{3}+u_f(t-\tau)\right|^{\frac{1}{2}}-\left(\frac{1}{3}\right)^{\frac{1}{2}}\right) \approx \frac{\sqrt{3}}{2}u_f(t-\tau). \tag{32}$$

This produces a system of linear DDEs: $\mathrm{d}\mathbf{x}/\mathrm{d}t = \mathbf{L_1}\mathbf{x}(t) + \mathbf{L_2}\mathbf{x}(t-\tau)$, where $\mathbf{L_1}$ is a normal matrix and $\mathbf{L_2}$ is a non-normal matrix. It is possible to find the eigenvalues of this linear DDE system and to quantify the non-normality of $\mathbf{L_2}$ but, in Balasubramanian and Sujith[36] and this article, a second linearization is performed on the time delay

$$\begin{aligned} u_f(t-\tau) &\approx u_f(t) - \tau\frac{\partial u_f(t)}{\partial t} \\ &= \sum_{k=1}^{N}\eta_k(t)\cos(k\pi x_f) - \tau\sum_{k=1}^{N}k\pi\left(\frac{\dot{\eta}_k(t)}{k\pi}\right)\cos(k\pi x_f) \end{aligned} \tag{33}$$

This linearization is valid only for the Galerkin modes for which $\tau \ll T_j$, where $T_j = 2/j$ is the period of the j^{th} Galerkin mode. Equations (32) and (33) are substituted into equation (25) to give the linearized governing equations

$$F_{1G} \equiv \frac{\mathrm{d}}{\mathrm{d}t}\eta_j - j\pi\left(\frac{\dot{\eta}_j}{j\pi}\right) = 0, \tag{34}$$

$$\begin{aligned} F_{2G} \equiv \frac{\mathrm{d}}{\mathrm{d}t}\left(\frac{\dot{\eta}_j}{j\pi}\right) + j\pi\eta_j + \zeta_j\left(\frac{\dot{\eta}_j}{j\pi}\right)\cdots \\ \cdots + \sqrt{3}\beta s_j\sum_{k=1}^{N}\eta_k(t)c_k - \sqrt{3}\beta\tau s_j\sum_{k=1}^{N}k\pi\left(\frac{\dot{\eta}_k}{k\pi}\right)c_k = 0 \end{aligned} \tag{35}$$

where $s_j \equiv \sin(j\pi x_f)$ and $c_k \equiv \cos(k\pi x_f)$. This is a set of linear ordinary differential equations (ODEs), which can be expressed in the matrix form

$$\frac{\mathrm{d}}{\mathrm{d}t}\mathbf{x} = \frac{\mathrm{d}}{\mathrm{d}t}\begin{pmatrix}\mathbf{u}\\ \mathbf{p}\end{pmatrix} = \begin{pmatrix}\mathbf{L}_{TL} & \mathbf{L}_{TR}\\ \mathbf{L}_{BL} & \mathbf{L}_{BR}\end{pmatrix}\begin{pmatrix}\mathbf{u}\\ \mathbf{p}\end{pmatrix} = \mathbf{L}\mathbf{x}. \tag{36}$$

L_{TR} and L_{BL} contain non-zero elements along their diagonals, which represent the isentropic part of the acoustics (i.e., the first two terms on the RHS of equations (36) and (37). L_{BR} contains nonzero elements along its diagonal, which represents the damping, ζ_j. The heat release term, β, makes every element nonzero in L_{BL} and L_{BR}. Therefore these two submatrices are full.

The rate of change of energy $\mathrm{d}E/\mathrm{d}t$ can be found either by substituting equations (32) and (33) into equation (31) or by evaluating $\mathbf{x}^T\mathbf{L}\mathbf{x}$. This gives

$$\begin{aligned} \frac{\mathrm{d}E}{\mathrm{d}t} = &-\sum_{j=1}^{N}\zeta_j\left(\frac{\dot{\eta}_j}{j\pi}\right)^2 - \sqrt{3}\beta\sum_{j=1}^{N}\sum_{k=1}^{N}s_jc_k\left(\frac{\dot{\eta}_j}{j\pi}\right)\eta_k \\ &+ \sqrt{3}\beta\tau\sum_{j=1}^{N}\sum_{k=1}^{N}s_jc_kk\pi\left(\frac{\dot{\eta}_j}{j\pi}\right)\left(\frac{\dot{\eta}_k}{k\pi}\right). \end{aligned} \tag{37}$$

Transient growth and triggering in the Rijke tube

The thermoacoustic system examined in this article has $x_f = 0.3$, $c_1 = 0.05$, $c_2 = 0.01$, $\tau = 0.02$, and $N = 10$. The time delay is slightly shorter than that found in Heckl,[22] who used $\tau = 0.08$. It models a hot wire and is therefore much shorter than it would be if modelling a flame. We chose a short delay so that the linearization equation (33) would be valid, even though we only use that linearization here. A longer time delay would cause the system to become unstable at lower β but would not change its qualitative behavior.

Fixed points and periodic solutions

The bifurcation diagram in Figure 10 shows the minimum acoustic energy on each periodic solution as a function of β. The Hopf bifurcation lies at $\beta_l = 0.86$ and is subcritical. The fold point lies at $\beta_c = 0.72$. There is an unstable periodic solution at low amplitude and a stable periodic solution at high amplitude. The results in this article are found for $\beta = 0.75$, at which the system has a stable fixed point, an unstable periodic solution and a stable periodic solution.

Non-normality and transient growth around the fixed point

When the governing equations are linearized around the fixed point, the evolution matrix equation (36) is

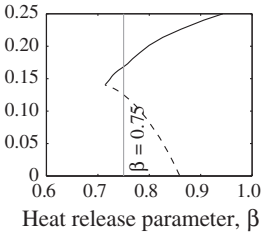


Figure 10. Bifurcation diagram for the Rijke tube.

obtained. The spectra and pseudospectra of this matrix are shown in Figure 11. The pseudospectra are nearly concentric circles centered on the spectra, which shows that the degree of non-normality is small.

The maximum transient growth, $G(T)$, can be calculated with the SVD, as described in section 3.1.1 and is shown in Figure 12. The maximum is at $G_{max} = 1.26$ and $T = 0.2$ and the corresponding initial state is shown in Figure 13.

Three significant points can be made at this stage. The first is that the amount of transient growth is small because the degree of non-normality is small. The second is that the maximum transient growth occurs within the first period ($0 < T < 2$), which will always be the case for a linearly stable system. The third is that, although the first mode ($\mathbf{u}_1^2 + \mathbf{p}_1^2$) has the highest initial amplitude, the next few modes have quite high initial amplitudes. This distribution differs considerably from the nonlinear optimal initial state in §5.4.

The most important question, however, is whether the transient growth from this initial state is sufficient to cause triggering to the stable periodic solution. Figure 14 shows the evolution of acoustic energy with time, starting from this initial state at different initial energies, E_0. The evolution is shown for the nonlinear governing equations (24) and (25) and the linear governing equations (34) and (35). At low E_0, the evolution is predicted well by the linear analysis but at high E_0 the nonlinear evolution has much less transient growth than the linear evolution.

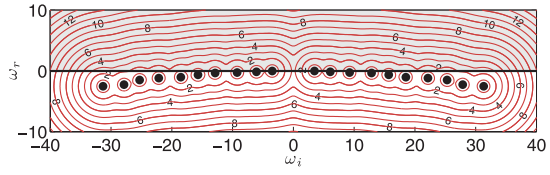


Figure 11. Spectra (black dots) and pseudospectra (contours) for linear perturbations about the fixed point.

Reading from Figure 10, the lowest energy on the unstable periodic solution is 0.125, which is a first approximation for the initial energy, E_0, required for triggering.[18] It will be shown that the lowest initial energy that leads to triggering is $E_0 = 0.1099$. At this value of E_0, the linear optimal (Figure 13) causes very little transient growth and, as will be confirmed later, is very different from the types of initial states that cause triggering. We might have anticipated this from Wicker et al.'s results,[18] who found that the initial state that triggers (in their two mode system) has to have most of its energy in the first mode.

Non-normality and transient growth around the unstable periodic solution

Non-normality and transient growth are usually considered only around fixed points. They can also be considered around periodic solutions, however, and this turns out to be crucial for triggering.

The 10 mode Rijke tube has 20 degrees of freedom. The state of the system can be represented by a point in 20-dimensional space and the acoustic energy of each point is given by its distance from the origin. This is difficult to draw so Figure 15 shows a cartoon of this

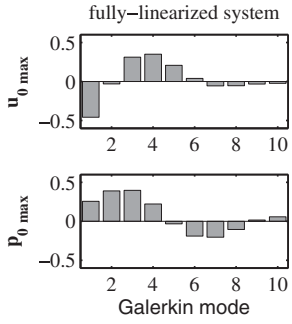


Figure 13. Amplitudes of the Galerkin modes that cause the maximum transient growth in Figure 12.

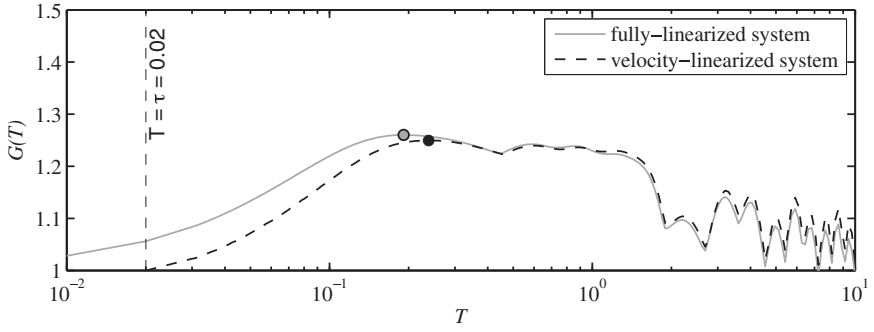


Figure 12. Maximum transient growth, $G(T)$, as a function of optimization time, T, for the 10 mode Rijke tube with $x_f = 0.3$, $c_1 = 0.05$, $c_2 = 0.01$, $\tau = 0.02$, and $\beta = 0.75$ for the fully-linearized system (solid line). The maximum value is $G_{max} = 1.26$ at $T = 0.2$.

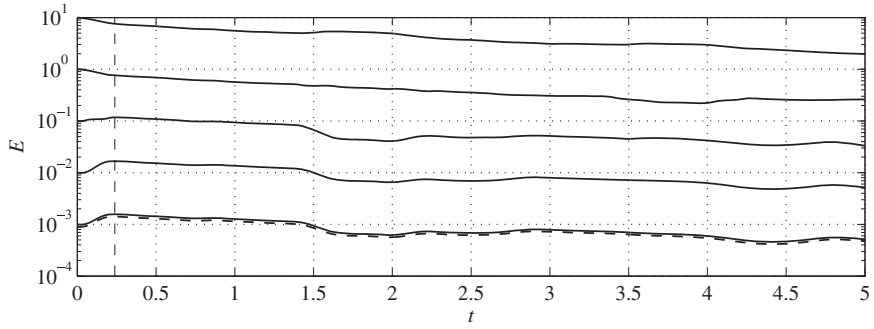


Figure 14. The acoustic energy growth with time, starting from the linear optimal initial state. The linear evolution is shown as a dashed line. The nonlinear evolution is shown as solid lines for initial acoustic energies of 10^{-3},10^{-2},10^{-1},1,10. For small initial energies, the nonlinear and linear evolutions are almost identical and transient growth can be seen at small times. For large initial energies, however, the nonlinear evolution differs greatly from the linear evolution. Crucially, it can be seen that the linear optimal initial state causes no transient growth at all here when the initial energy is greater than 1.

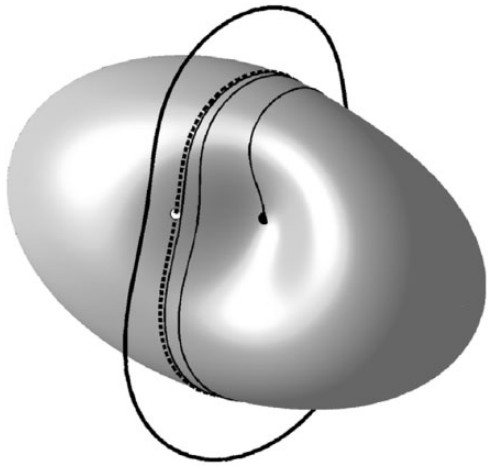


Figure 15. A cartoon of the manifold that separates the states that evolve to the stable fixed point from those that evolve to the stable periodic solution.
Figure reproduced from [33], with permission.

space in three dimensions. The grey potato-shaped surface is the closed manifold that separates the states that evolve to the stable fixed point, which lies inside the surface, from the states that evolve to the stable periodic solution, which is the large loop that lies away from the surface. Points *exactly* on the manifold remain on the manifold for all time. In order for a state to reach the stable periodic solution, it must start outside this closed manifold.

The unstable periodic solution is a loop exactly on this manifold. Any state on this loop, if given an infinitesimal increase in energy, would evolve to the stable periodic solution. This is why the lowest energy point on this loop is a first approximation to the energy required for triggering. We will call this point $\mathbf{n}$ and define the unit vector from the origin to this point as $\hat{\mathbf{n}}$. The important question is whether there are states with even lower energy that lie outside this closed manifold. In other words, what is the shape of the potato around the unstable periodic solution?

Let us consider small perturbations around the unstable periodic solution. We do this by generating the monodromy matrix[32] which maps the evolution of an infinitesimal perturbation after one loop around the periodic solution. Its eigenvalues and pseudospectra are shown in Figure 16. The pseudospectra are nearly (but not quite) circles centered on the spectra. Therefore, the system is slightly non-normal. There are eighteen eigenvalues inside the unit circle, which are stable, one eigenvalue on the unit circle, which is neutrally stable and represents motion in the direction of the periodic solution, and one eigenvalue outside the unit circle, which is unstable. This shows that the unstable manifold attracts states from every direction except one. Furthermore, because this system has no other fixed, periodic, or chaotic solutions, every state exactly on the manifold, as well as remaining on the manifold, must be attracted toward the unstable periodic solution.

At the point with minimum energy on the unstable periodic solution, the neutral eigenvector is perpendicular to the radial direction, $\hat{\mathbf{n}}$, If the monodromy matrix is normal and if the unstable eigenvector points in direction $\hat{\mathbf{n}}$, then all the stable eigenvectors must also be perpendicular to the radial direction there. This means that the point with minimum energy on the unstable periodic solution is a local energy minimum on the manifold.

If the monodromy matrix is non-normal, however, then the stable eigenvectors are nonorthogonal. Whichever direction the unstable eigenvector points in, the stable eigenvectors are unlikely to point perpendicular to the radial direction, $\hat{\mathbf{n}}$. This means that the point with minimum energy on the unstable periodic solution is not a local energy minimum on the manifold. It is easy to check this numerically for specific cases by taking the dot product of the stable

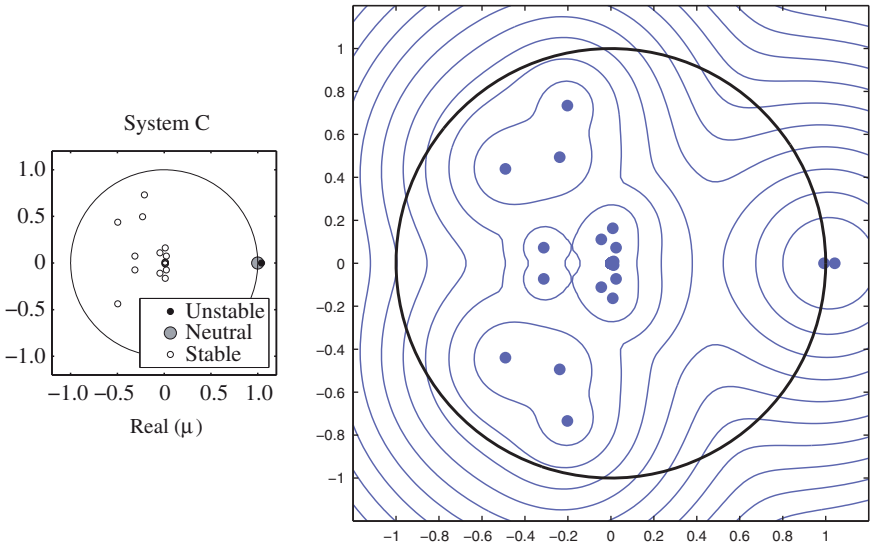


Figure 16. (a) Eigenvalues and (b) pseudospectra of the monodromy matrix around the unstable periodic solution.

eigenvectors with the radial direction $\hat{\mathbf{n}}$. The technique described in the next section and Juniper[33] can then be used to iterate to the local energy minimum. It uses a local optimization routine and starts from the lowest energy point on the unstable periodic solution.

Although this is enough motivation for the analysis in the next section, we may wish to use this linear technique to estimate the optimum initial state very crudely.

Firstly, let us consider states that remain exactly on the manifold. In the long time limit, all of these states are attracted to the unstable periodic solution. If the monodromy matrix is non-normal, however, some states initially grow away from the unstable periodic solution, some to higher energies, before being attracted back. These states are the projection of the first singular vector of the monodromy matrix, $\mathbf{s}$, onto the manifold around the unstable periodic solution. This direction is $(\mathbf{s} - \mathbf{s} \cdot \hat{\mathbf{n}})$. It is also easy to check this numerically.

Secondly, if we make the reasonable assumption that trajectories are locally parallel, then the states that start from lower energy than the unstable periodic solution but grow transiently and are then attracted toward it will look similar to those described above. To a first approximation, therefore, the optimal initial state is given by $\mathbf{n} + k(\mathbf{s} - \mathbf{s} \cdot \hat{\mathbf{n}})$, where k is an unknown small value.

It is shown in Juniper[33] that $\mathbf{n}$ has most energy in the first mode and that $\mathbf{s}$ has most energy in the first mode and appreciable energy in the third and fourth modes. We would expect, therefore, that the optimal initial state will have most energy in the first mode and some in the third and fourth, but not as much in the second mode. This is what is found in the next section.

Nonlinear optimal initial states and triggering

Our analysis of non-normality and transient growth around the fixed point calculated the perturbations that maximize transient growth around the unstable periodic solution and shows that some initial states that trigger can have lower energy than the unstable periodic solution. It gives an indication of the direction of these points away from the unstable periodic solution but cannot give the optimal initial state itself. For that, nonlinear optimization is required.

In the linear analysis, the energy growth, G, is a function only of the optimization time, T. In the nonlinear analysis, it is also a function of the state's initial amplitude, which can be quantified by the initial acoustic energy, E_0. Therefore, G_{max} needs to be found by optimizing G over all T and all E_0.

These nonlinear optimal initial states are found with a constrained optimization technique[33] adapted from optimal control.[93] A cost functional, $\mathcal{J}$, is defined, which can be $\|\mathbf{x}(T)\|^2/\|\mathbf{x}_0\|^2$. A Lagrangian functional, $\mathcal{L}$, is then defined as the cost functional, $\mathcal{J}$, minus a set of inner products. These inner products multiply the governing equations by one set of Lagrange multipliers and the initial state by another set of Lagrange multipliers. When all variations of $\mathcal{L}$ with respect to the Lagrange multipliers, state variables, $\mathbf{x}$, and initial state, $\mathbf{x}_0$, are zero then an initial state has been found that optimizes $\mathcal{J}$ and satisfies the governing equations.

To find this initial state, the direct governing equations are integrated forward for time T from an initial guess, thus satisfying the requirement that all variations of $\mathcal{L}$ with respect to the Lagrange multipliers are zero. The Lagrangian functional is then re-arranged so that it

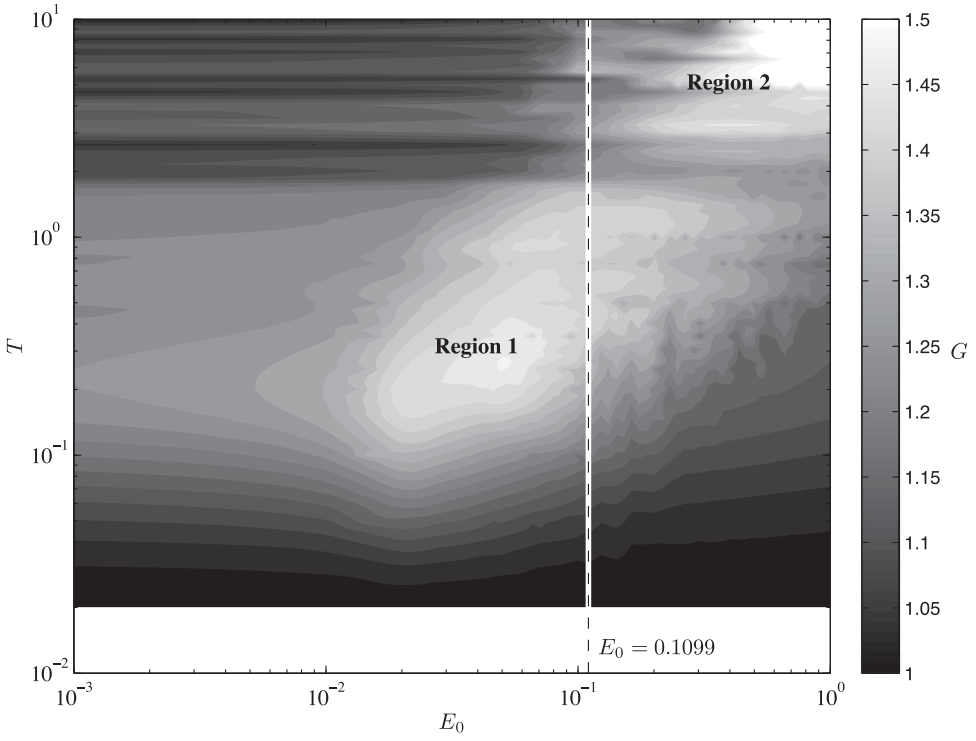


Figure 17. Transient growth, $G(T,E_0)$, as a function of optimization time, T and initial energy, E_0, for perturbations around the fixed point of the Rijke tube.

is expressed in terms of a different set of inner products. These inner products multiply the state variables, $\mathbf{x}$, by a first set of constraints. They also multiply the initial state, $\mathbf{x}_0$, by a second set of constraints. The requirement that all variations of $\mathcal{L}$ with respect to $\mathbf{x}$ are zero can be met by satisfying the first constraints. Half of these, known as the *optimality conditions*, determine the relationship between an adjoint state vector, $\mathbf{x}^+$, and the direct state vector, $\mathbf{x}$, at time T. The other half, known as the *adjoint* governing equations, govern the evolution of $\mathbf{x}^+$ for $t = [0, T]$. After setting the optimality conditions at $t = T$, the adjoint governing equations are integrated backward to time 0, thus satisfying the requirement that all variations of $\mathcal{L}$ with respect to $\mathbf{x}$ are zero. The second set of constraints return the gradient information $\partial\mathcal{L}/\partial\mathbf{x_0}$ at the initial guess for $\mathbf{x}_0$. This is combined with a convenient optimization algorithm, such as the steepest descent method or the conjugate gradient method, in order to converge toward the optimal initial state, at which $\partial\mathcal{L}/\partial\mathbf{x_0} = 0$. This finds local optima. This process is repeated starting from several hundred random starting states in order to find a global optimum.

Figure 17 shows contours of $G(T, E_0)$. For details, please refer Juniper.[33] Two regions of high transient growth can be seen. The first is centered on $(E_0, T) = (0.050, 0.25)$, with $G_{max} = 1.48$, and is a continuation of the linear optimal into the non-linear regime. The second is found at high values of T and corresponds to initial states that reach the stable limit cycle from the lowest possible energies. These are the triggering states that we seek. The lowest energy state that triggers has $E_0 = 1.099$ and it is not a continuation of the linear optimal.

Figure 18 shows a slice through Figure 17 at $E_0 = 0.1099$ and Figure 19 shows the corresponding initial states at optimization times $T = 0.1$, $T = 1.0$, and $T = 10$. Figure 20 shows the evolution from these three initial states on two timescales: (a) $0 \leq t \leq 10$ (b) $0 \leq t \leq 100$. The first state ($T = 0.1$), which we show because its optimization time is similar to the linear optimal time, has strong initial transient growth but then very quickly decays back to the fixed point. The second state ($T = 1$), which is in region 1 of Figure 17, has strong growth over the first cycle and is almost attracted toward the unstable periodic solution but then also decays back to the fixed point. The third state ($T = 10$), which is in region 2 of Figure 17, has less growth over the first cycle but is then attracted toward the unstable periodic solution and, although not shown here, is then attracted to the stable periodic solution. This state has most of its energy in the first mode, as anticipated from Wicker et al.,[18] so that it can start reasonably close to the unstable periodic solution. It has significant energy in the third and fourth modes, as suggested by the linear analysis around the unstable periodic solution.

Jagadesan and Sujith[31] showed experimentally that during triggering, the system evolves transiently toward

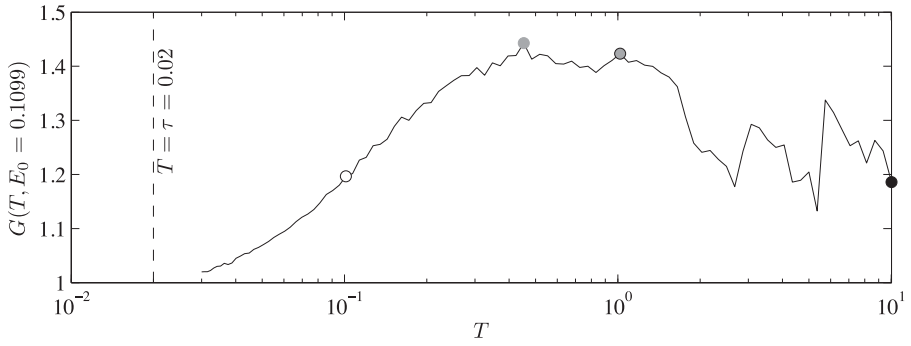


Figure 18. Slice through Figure 17 at $E_0 = 0.1099$.

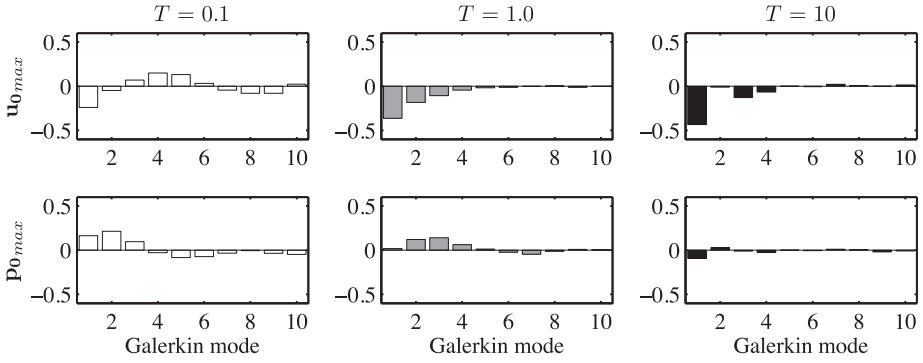


Figure 19. Initial states that give maximum transient growth at $E_0 = 0.1099$ for $T = 0.1$, $T = 1.0$, and $T = 10$. The optimal initial state with $T = 10$ has most energy in the first mode and appreciable energy in the third and fourth modes.

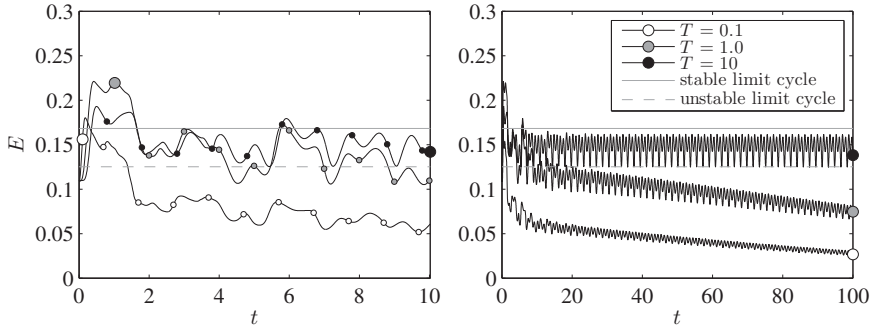


Figure 20. Energy, E, as a function of time, t, for the three initial states in Figure 19. The optimal initial state with $T = 10$ has smaller transient growth at short times but then grows to the stable limit cycle (not shown).

an unstable periodic orbit, before growing to limit-cycle, in a manner analogous to this bypass scenario originally proposed by Juniper.[33]

Non-normality and transient growth in complex systems

Having discussed a toy model for Rijke tube in great detail, more complex models for the Rijke tube and other thermoacoustic systems can be constructed. We will now briefly review the studies on systems that are more complex.

Ducted premixed flame

Stringent emission requirements drive operating conditions of premixed gas turbines and combustors to the lean regime. However, lean premixed combustion

has been shown to be particularly susceptible to combustion instability.[94,95] Subramanian and Sujith[39] investigated the role of non-normality and nonlinearity in flame-acoustic interaction in a ducted premixed flame.

The premixed flame thermoacoustic system is modeled by considering the acoustic momentum and energy equations together with the equation for the evolution of the flame front obtained from the kinematic G-equation.[96] The G-equation is rewritten as the front-tracking equation as given in equation (39) for an axi-symmetric wedge flame in a purely axial flow[45] shown in Figure 21. The scales used for nondimensionalization are derived from the length of the flame $b \sin\alpha$ and the velocity of the flow $\bar{u}$ as shown below in equation (38).

$$X = \tilde{X}\sin\alpha/b; \quad \bar{u} = \tilde{\bar{u}}/\tilde{\bar{u}} = 1; \quad t = \tilde{t}/(b/\bar{u}\sin\alpha) \quad (38)$$

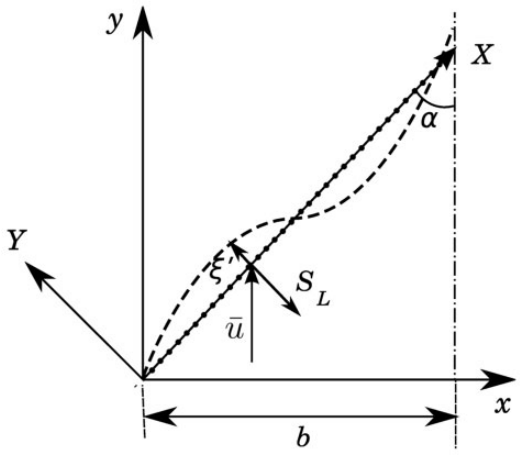


Figure 21. Geometry of an axi-symmetric wedge flame stabilized on a wire. Here ξ' is the displacement of instantaneous flame shape from the unperturbed flame shape along X, α is the flame angle, S_L is the laminar flame speed, b is the radius of the burner, and $\bar{u}$ is the mean flow. Figure reproduced with permission from Subramanian and Sujith.[39]

$$\frac{\partial\xi'}{\partial t} = (1+u')\cos\alpha\left(\frac{\partial\xi'}{\partial X}\right) - (1+u')\sin\alpha - \sqrt{1+\left(\frac{\partial\xi'}{\partial X}\right)^2} \quad (39)$$

The configuration of a duct which is open at both ends with the axi-symmetric wedge flame stabilized at an axial location within it is considered, see Figure 22.

The linear operator of a generic thermoacoustic system has been shown to be non-normal.[35,36] The linearized operator for the premixed flame thermoacoustic system is also found to be non-normal leading to non-orthogonality of its eigenvectors.[39] Nonorthogonal eigenvectors can cause transient growth in evolutions even when all the eigenvectors are decaying for a linearly stable case. Therefore, classical linear stability theory cannot predict the finite time transient growth observed in non-normal systems. A parametric study of the variation in transient growth due to change in parameters such as flame location and flame angle is performed. It is found that the transient growth is pronounced when the flame has a small angle of flame and is located close to the center of the duct. The optimum initial condition which causes maximum transient growth can be identified using SVD for a given system configuration. In addition to projections along the acoustic variables of velocity and pressure, the optimal initial condition for the self evolving system has significant projections along the variables for heat release rate.

Nonlinear simulations show subcritical transition to instability from a small but finite amplitude perturbation to the system as shown in Figure 23. The system is perturbed with the optimal initial perturbation with initial acoustic velocity of small but finite amplitude at the flame location. It shows that the linear and nonlinear evolutions diverge within a short period of time. Asymptotically, the linear evolution decays as shown in Figure 23(a) while the nonlinear evolution reaches a self sustained oscillation of amplitude as seen in the inset from Figure 23(b). Therefore, an initial condition

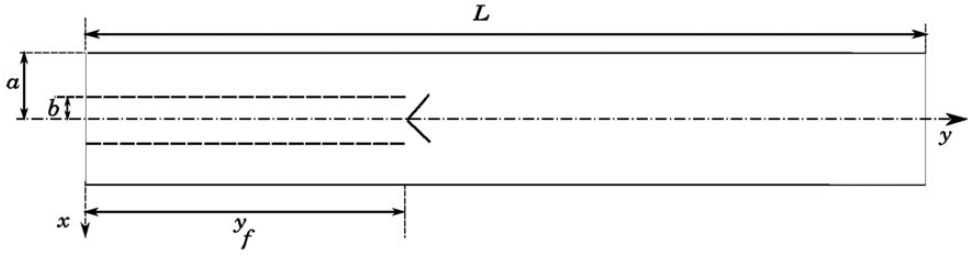


Figure 22. Geometry of coupled system with an axi-symmetric wedge flame stabilized on a wire. Here, L is the length of the duct, (b/a) is the ratio of burner to duct radius and $\tilde{y}_f$ is the flame location along the length of the duct. Figure reproduced with permission from Subramanian and Sujith.[39]

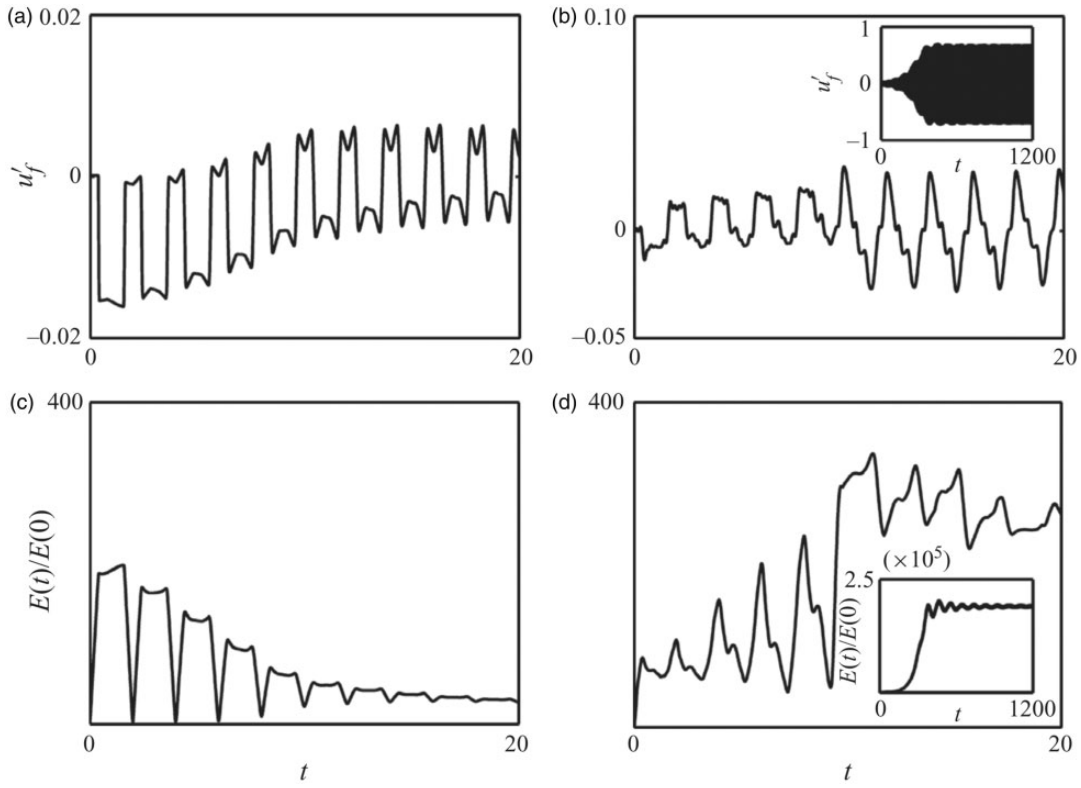


Figure 23. Evolution of acoustic velocity at the flame for (a) linearised system and (b) nonlinear system. Evolution of the energy due to fluctuations $E(t)/E(0)$ for (c) linearised system and (d) nonlinear system. All evolutions are plotted along the acoustic time scale t. The optimal initial condition with $u'_f(0) = 7.8 \times 10^{-5}$ and $E(0) = 4 \times 10^{-6}$ is seen to grow transiently and decay in the linear evolution. The nonlinear evolution reaches a limit cycle of amplitude $|u'_f|_{LC} = 0.67$. The other system parameters are $\alpha = 10^{\circ}$, $y_f = 0.2$, $\phi = 0.8$, $c_1 = 2 \times 10^{-3}$, $c_2 = 2 \times 10^{-4}$, $S_L = 0.2782\ m/s$ and $\Delta q_R = 2.2263 \times 10^6\ J/Kg$. Figure reproduced with permission from Subramanian and Sujith.[39]

with very small initial amplitude, if applied in the optimal manner, can cause transient growth in the energy of the system.

The premixed flame thermoacoustic system has more degrees of freedom than the number of acoustic modes. These additional degrees of freedom represent the internal degrees of freedom of the flame front or the internal flame dynamics. These internal degrees of the flame front must be preserved in the thermoacoustic model to accurately capture the non-normal effects. In thermoacoustic systems, subcritical transition to instability has been thought of as being caused by a large amplitude initial perturbation to a linearly stable system. In a linearly stable case, even a small but finite amplitude optimal initial perturbation is shown to reach a limit cycle. The optimum initial condition may have contributions from variables that represent the flame front dynamics, and will not be purely acoustic. Therefore in non-normal systems, initial perturbations with amplitudes that are small when compared with the limit cycle oscillations can cause subcritical transition to instability.

Ducted diffusion flame

The role of non-normality and nonlinearity in flame-acoustic interaction in a ducted diffusion flame has been investigated by Balasubramanian and Sujith.[35] They used the infinite rate chemistry model to study unsteady diffusion flames in a Burke–Schumann type geometry. The combustion response to perturbations of velocity is non-normal and nonlinear. This flame model is then coupled with a linear model of the duct acoustic field to study the temporal evolution of acoustic perturbations. The one-dimensional acoustic field is simulated in the time domain using the Galerkin technique, treating the fluctuating heat release from the combustion zone as a compact acoustic source. The coupled combustion-acoustic system is non-normal and nonlinear.

Solid rocket motor

SRMs are often prone to combustion instability. The prediction of combustion instability in the early design stage is a formidable task due to the complex unsteady

flow field existing in the combustion chamber. Combustion instability occurs when the unsteady burn rate from the propellant (in SRMs) is amplified by the positive feed back of the acoustic oscillations in the chamber. Combustion instability causes excessive pressure oscillations, which might resonate with the structural modes of the rocket, leading to excessive vibration and damage of the payload. Further, during the occurrence of combustion instability, the heat transfer to the combustion chamber walls is increased, eventually melting them.[2] Instabilities in SRMs have been known to exist since 1930.[2] Since then, many investigations were conducted to understand the mechanisms behind them and arrive at measures to control them.

Mariappan and Sujith[42] investigated the role of non-normality in the occurrence of triggering instability in SRMs with homogeneous propellant grain. Their theoretical analysis starts with linearizing the governing equations and analyzing their stability. This leads to finding the eigenvalues (complex frequency) and eigenmodes of the system. In classical linear stability analysis, a system is said to be linearly stable if the oscillations decay to zero in the asymptotic time limit, reaching finally the steady state (stable fixed point). The system is linearly unstable if the oscillations grow exponentially. Both the definitions are for small disturbances with respect to the corresponding mean quantities. Non-normal systems show initial transient growth for suitable initial perturbations even when the system is stable according to classical linear stability theory. Transient growth plays an important role in the subcritical transition to instability regime.[42] In SRM the above is termed as pulsed instability, where the system is linearly (small amplitude) stable, but nonlinearly (large amplitude) unstable.

Mariappan and Sujith[42] showed that pulsed instabilities can occur in two ways: (1) by introducing a large pulse into the system where nonlinearities are important, leading to a limit cycle; (2) through a small, but not infinitesimal, initial condition in the appropriate direction that causes transient growth. As the amplitude of the oscillation increases, nonlinear terms can then contribute, leading to a limit cycle.

Experimental efforts

The ideas of non-normality and transient growth have been pursued by the fluid dynamics community for nearly two decades, resulting in a large body of theoretical and numerical studies in the literature. However, there are just a handful of experimental efforts. The lack of experimental studies, in the authors' opinion, is due to the inherent difficulty in extracting the relevant details (e.g., the growth factor) from experiments.

Mariappan et al.[44] confirmed experimentally that the eigenmodes of a horizontal Rijke tube are non-orthogonal. Further, they quantified transient growth using acoustic energy as a scalar norm, and confirmed the predictions of Balasubramanian and Sujith[36] and Juniper.[33] Kim and Hochgreb[47] experimentally investigated triggering and transient growth of thermoacoustic oscillations in a model lean-premixed gas turbine combustor. Zhao[46,97] investigated transient growth of flow disturbances in triggering combustion instability in a Rijke tube that is driven by a premixed flame.

Characterizing bifurcations in thermoacoustic systems

We have seen the role played by non-normality and transient growth in the evolution of a thermoacoustic system. The final state to which the system evolved depends on the nonlinear characteristics of the system.

The nonlinear dynamical behavior of a thermoacoustic system is best characterized by a bifurcation diagram. The bifurcation diagram can be obtained theoretically, numerically and experimentally.

Method of multiple scales

Analytical methods of bifurcation analysis are particularly advantageous as they help to (1) identify unifying common features across varied systems and to (2) derive reduced order models that preserve the nonlinear dynamical behavior of the system. Classical linear stability analysis is employed to determine the onset of instabilities in thermoacoustic systems. A weakly nonlinear analysis near the onset of linear instability through a Hopf point can be performed using the method of multiple scales. This method helps to extend the results of linear analysis in determining the criticality of the Hopf bifurcation by characterizing the branch of periodic solutions that emerge from the Hopf point. Subramanian et al.[98] applied the method of multiple scales to study subcritical bifurcations and bistability in thermoacoustic systems.

The method of multiple scales consists of introducing different scales to formally separate the fast and slow scales.[99] The dynamics of a general thermoacoustic system is analyzed close to the critical Hopf point that occurs at a parameter value of $\sigma = \sigma_H$. The fast timescale (reciprocal of the frequency) and the location of the Hopf point can be obtained from linear stability analysis. The evolution equation of the system close to this critical point can then be completely described in terms of a complex amplitude W that varies only in the slow time scale t. The evolution of W in the slow time scale is in the form of a Stuart–Landau equation[100] given by

$$\frac{\mathrm{d}W}{dt} = (B_1 + iB_3)(\sigma - \sigma_H)W + (B_2 + iB_4)|W|^2 W \quad (40)$$

Expanding $W = Ae^{i\phi}$ in the above equation, the amplitude and phase equations for the evolution of the system can be obtained as

$$\frac{dA}{dt} = (B_1\, \nu)\, A + B_2\, A^3\,, \tag{41}$$

$$\frac{d\phi}{dt} = B_3\, \nu + B_4\, A^2. \tag{42}$$

In the above relations, determining the fixed point of the slow flow amplitude equation (41) gives the amplitude of the periodic state and the stability analysis of the fixed point helps in determining the criticality of the Hopf bifurcation. However, the estimates obtained using this method become less accurate as we move away from the Hopf point as the assumption of weak nonlinearity becomes invalid. Other analytical methods such as harmonic balance or energy balance method[101] must then be employed to estimate the dynamical behavior of the system far from the Hopf point. Alternatively, numerical methods of continuation can be used to obtain the complete bifurcation plots of systems using a single technique as detailed in the next subsection.

Numerical continuation

The nonlinear dynamical behavior of a thermoacoustic system is best characterized by a bifurcation diagram. Numerical continuation is used to compute the numerical solutions to a set of parameterized nonlinear equations where other approaches to solve the problem are prohibitively expensive. The limit cycles found by continuation methods are exact, because the methods operate in the time domain. Frequency domain methods, such as the flame describing function (FDF), can only estimate limit cycles. More importantly, however, continuation analysis can be used as a tool to gain insight into the qualitative properties of the solutions. It is used to calculate the bifurcations or qualitative changes in the solution for the variation of one or more parameters of the system. Solutions which are connected to a given state of the system are computed. Bifurcations are identified by including multiple test functions which change sign at the critical value of the parameter.

This method has the advantage that once a stationary or periodic solution has been computed, the dependence of the solution on the variation of a parameter is obtained very efficiently. It can also be used to compute unstable limit cycles. Presently, this technique has been applied to thermoacoustic systems such as a nonlinear Rijke tube model[102] and to the ducted premixed flame model.[103]

Using iterative techniques,[54] continuation methods have now been applied to a Burke–Schumann flame in an acoustic duct with a few hundred degrees of freedom[53] and to a G-equation flame in an acoustic duct with a few thousand degrees of freedom.[104] By examining the Floquet multipliers of the periodic solutions that are found, this reveals stable periodic solutions, unstable periodic solutions, stable and unstable period-2 periodic solutions, Hopf bifurcations, Neimark–Sacker bifurcations, fold bifurcations, and period-doubling bifurcations. This qualitatively shows the same rich nonlinear behavior seen in experiments.[8] Continuation methods can find unstable solutions as easily as they can find stable solutions. In regions of multistability, these unstable solutions have been shown to be critical for mode switching.[30,31] Furthermore, the corresponding Floquet modes show which coupled behavior is responsible for causing each bifurcation.

Conclusions

A thermoacoustic system is non-normal, and hence the eigenvectors are nonorthogonal. Non-normality leads to short time amplification, even though the individual modes decay exponentially. In a thermoacoustic system, states that have low energy can initially exploit non-normal linear transient growth around the unstable periodic solution before growing from there to the stable periodic solution due to nonlinear effects. This can explain the triggering caused by small-amplitude disturbances, or the order of background noise level.[3] The current methodology to study the onset of thermoacoustic oscillations involves looking for exponentially growing or decaying modes by calculating the individual eigenvalues of the linearized system. More sophisticated approaches have to be adoped and more involved methods have to be introduced, to accurately capture the transient behavior which is critical for the overall system stability. We wish to emphasize that thermoacoustic systems are indeed nonlinear dynamical systems and should be analyzed with tools from that field that are well developed.

Presently, thermoacoustic instability is associated synonymously with limit cycle oscillations.[3] However, recent results indicate that the dynamics of thermoacoustic oscillations are not limited to limit cycle oscillations. The limit cycle state obtained at the onset of instability can undergo further bifurcations leading to a variety of complex nonlinear states. The quasi-periodic route to chaos[7] and the frequency-locking route to chaos[8] have been recently established in thermoacoustics. Further Kabiraj et al.[9,105] has also identified type-II intermittancy in thermoacoustic instabilities. Models of thermoacoustics of ducted premixed flames also capture this phenomena.[103,106] In combustors with turbulent flow, Nair et al.[107] showed recently that the onset of combustion-driven oscillations is always

presaged by intermittent bursts of high amplitude periodic oscillations that appear in a near-random fashion amidst regions of aperiodic low-amplitude fluctuations. Further, Nair and Sujith[108] showed that in a turbulent combustor the low-amplitude, irregular pressure fluctuations acquired during stable regimes, termed combustion noise, display scale invariance and have a multifractal signature that disappears at the onset of combustion instability. Thus it appears as if the subject of nonlinear thermoacoustics is headed for exiting developments.

Acknowledgements

This article had its inception in the summer of 2010, when all the three authors were at the Institute for Advanced Study (IAS) of TU Munich. We thank the IAS, TUM for its generous and flexible support of this work. We are also grateful to Wolfgang Polifke for welcoming us to TUM and for his kind support.

Declaration of conflicting interests

The author(s) declared no potential conflicts of interest with respect to the research, authorship, and/or publication of this article.

Funding

The author(s) received no financial support for the research, authorship, and/or publication of this article.

References

1. Heppenheimer TA. *Countdown: a history of space flight*. New York: Wiley & sons, 1999.
2. Culick FEC. *Unsteady motions in combustion chambers for propulsion systems*. RTO AGARD-ograph, AG-AVT-039, 2006.
3. Zinn BT and Lieuwen TC. *Combustion instabilities: basic concepts. Combustion instabilities in gas turbine engines: operational experience, fundamental mechanisms, and modeling, Chapter 1*. Progress in Astronautics and Aeronautics, AIAA, 2005.
4. Marble FE and Candel SM. Acoustic disturbance from gas nonuniformities convected through a nozzle). *J Sound Vibration* 1977; 55: 225–243.
5. Sterling JD and Zukoski EE. Nonlinear dynamics of laboratory combustor pressure oscillations. *Combust Sci Technol* 1991; 77: 225–238.
6. Sterling JD. Nonlinear analysis and modelling of combustion instabilities in a laboratory combustor. *Combust Sci Technol* 1993; 89: 167–179.
7. Kabiraj L, Saurabh A, Wahi P, et al. Route to chaos for combustion instability in ducted laminar premixed flames. *Chaos* 2012; 22: 023129.
8. Kabiraj L, Sujith RI and Wahi P. Bifurcations of self-excited ducted laminar premixed flames. *J Eng Gas Turb Power* 2012; 134: 031502.
9. Kabiraj L and Sujith RI. Nonlinear self-excited thermoacoustic oscillations: intermittency and flame blowoutt. *J Fluid Mech* 2012; 713: 376–397.
10. Lieuwen T. Experimental investigation of limit-cycle oscillations in an unstable gas turbine combustor. *J Propul Power* 2002; 18: 61–67.
11. Chu BT. Analysis of a self-sustained thermally driven nonlinear vibration. *Phys Fluids* 1963; 6: 1638–1644.
12. Culick FEC. Nonlinear growth and limiting amplitude of acoustic oscillations in combustion chambers. *Combust Sci Technol* 1971; 3: 1–16.
13. Awad E and Culick FEC. On the existence and stability of limit cycles for longitudinal acoustic modes in a combustion chamber. *Combust Sci Technol* 1986; 46: 195–222.
14. Flandro GA, Fischbach SR and Majdalani J. Nonlinear rocket motor stability prediction: limit amplitude, triggering, and mean pressure shift. *Phys Fluids* 2007; 19: 094101.
15. Paparizos LG and Culick FEC. The two-mode approximation to nonlinear acoustics in combustion chambers, i: exact solution for second order acoustics. *Combust Sci Technol* 1989; 65: 39–65.
16. Yang V, Kim SI and Culick FEC. Triggering of longitudinal pressure oscillations in combustion chambers. 1. Nonlinear gas dynamics. *Combust Sci Technol* 1986; 72: 183–214.
17. Ananthkrishnan N, Deo S and Culick FEC. Reduced order modelling and dynamics of nonlinear acoustic waves in a combustion chamber. *Combust Sci Technol* 2005; 177: 221–248.
18. Wicker JM, Kim SI, Greene WD, et al. Triggering of longitudinal combustion instabilities in rocket motors: nonlinear combustion response. *J Propul Power* 1996; 12: 1148–1158.
19. Baum JD, Levine JN and Lovine RL. Pulse-triggered instability in solid rocket motors. *AIAA J* 1984; 22: 1413.
20. Dowling AP. A kinematic model of a ducted flame. *J Fluid Mech* 1999; 394: 51–72.
21. Matveev KI. *Thermo-acoustic instabilities in the Rijke tube: Experiments and modeling*. PhD Thesis, California Institute of Technology, Pasadena, 2003.
22. Heckl MA. Nonlinear acoustic effects in the Rijke tube. *Acustica* 1990; 72: 63–71.
23. Hantschk CC and Vortmeyer D. Numerical simulation of self-excited thermo-acoustic instabilities in a Rijke tube. *J Sound Vibration* 1999; 277: 511–522.
24. Matveev KI. Energy consideration of the nonlinear effects in the Rijke tube. *J Fluids Struct* 2003; 18: 783–794.
25. Matveev KI and Culick FEC. A study of the transition to the instability in a Rijke tube with axial temperature gradient. *J Sound Vibration* 2003; 264: 689–706.
26. Yoon HG, Peddieson J and Purdy KR. Nonlinear response of a generalized Rijke tube. *Int J Eng Sci* 2001; 39: 1707–1723.
27. Dickinson LA. Command initiation of finite wave axial combustion instability in solid propellant rocket engines. *ARS J* 1962; 32: 643–644.
28. Mitchell CE, Crocco L and Sirignano WA. Nonlinear longitudinal instability in rocket motors with concentrated combustion. *Combust Sci Technol* 1969; 1: 35–64.

29. Zinn BT and Lores ME. Application of the Galerkin methods in the solution of nonlinear axial combustion instability problems in liquid rockets. *Combust Sci Technol* 1972; 4: 269–278.
30. Waugh IC and Juniper MP. Triggering in a thermoacoustic system with stochastic noise transition. *Int J Spray Combust Dyn* 2011; 3: 225–242.
31. Jagadesan V and Sujith RI. Experimental investigation of noise induced triggering in thermoacoustic systems. *Proc Combust Inst* 2012; 34: 3175–3183.
32. Schmid PJ. Nonmodal stability theory. *Ann Rev Fluid Mech* 2007; 39: 129–162.
33. Juniper MP. Triggering in the horizontal Rijke tube: non-normality, transient growth and bypass transition. *J Fluid Mech* 2011; 667: 272–308.
34. Nicoud F, Benoit L, Sensiau C, et al. Acoustic modes in combustors with complex impedances and multidimensional active flames. *AIAA J* 2007; 45: 426–441.
35. Balasubramanian K and Sujith RI. Nonnormality and nonlinearity in combustion-acoustic interaction in diffusion flames. *J Fluid Mech* 2008; 594: 29–57.
36. Balasubramanian K and Sujith RI. Thermoacoustic instability in a Rijke tube: Nonnormality and nonlinearity. *Phys Fluids* 2008; 20: 29–57.
37. Mariappan S, Schmid PJ and Sujith RI. Role of transient growth in subcritical transition to thermoacoustic instability in a Rijke tube. In *16th AIAA/CEAS Aeroacoustics Conference, June 7–10, Stockholm, Sweden*, 2010.
38. Mariappan S and Sujith RI. Modelling nonlinear thermoacoustic instability in an electrically heated Rijke tube. *J Fluid Mech* 2011; 680: 511–533.
39. Subramanian P and Sujith RI. Non-normality and internal flame dynamics in premixed flame acoustic interaction. *J Fluid Mech* 2011; 679: 315–342.
40. Balasubramanian K, Tulsyan B and Sujith RI. Revisiting a model for combustion instability involving vortex shedding. *Combust Sci Technol* 2009; 181: 457–482.
41. Kedia KS, Nagaraja SB and Sujith RI. Impact of linear coupling on thermoacoustic instabilities. *Combust Sci Technol* 2008; 180: 1588–1612.
42. Mariappan S and Sujith RI. Thermoacoustic instability in solid rocket motor—non-normality and nonlinear instabilities. *J Fluid Mech* 2010; 653: 1–33.
43. Kulkarni R, Balasubramanian K and Sujith RI. Non-normality and its consequences in active control of thermoacoustic instabilities. *J Fluid Mech* 2011; 670: 130–149.
44. Mariappan S, Sujith RI and Schmid PJ. Experimental investigation of non-normality and transient growth in thermoacoustic instabilities. In *47th AIAA/ASME/SAE/ASEE Joint Propulsion Conference and Exhibit*, San Diego, California, 31 July–3 August 2011.
45. Wieczoerk K, Sensiau C, Polifke W, et al. Assessing non-normal effects in thermoacoustic systems with mean flow. *Phys Fluids* 2011; 679: 107103.
46. Zhao D. Measurements of triggering and transient growth in a model lean-premixed gas turbine combustor. *Combust Flame* 2012; 159: 2126–2137.
47. Kim KT and Hochgreb S. Measurements of triggering and transient growth in a model lean-premixed gas turbine combustor. *Combust Flame* 2012; 159: 1215–1227.
48. Waugh IC, Geuss M and Juniper MP. Triggering, bypass transition and the effect of noise on a linearly stable thermoacoustic system. *Proc Combust Inst* 2011; 33: 2945–2952.
49. Mangesius H and Polifke W. A discrete-time, state-space approach for the investigation of non-normal effects in thermoacoustic systems. *Int J Spray Combust Dyn* 2011; 3: 331–350.
50. Fedotov S, Bashkirtseva I and Ryashko L. Stochastic analysis of a non-normal dynamical system mimicking a laminar-to-turbulent subcritical transition. *Phys Rev E* 2002; 66: 066310.
51. Giannetti F and Luchini P. Structural sensitivity of the first instability of the cylinder wake. *J Fluid Mech* 2007; 581: 167–197.
52. Jahnke CC and Culick FEC. Application of dynamical systems theory to nonlinear combustion instabilities. *J Propul Power* 1994; 10: 508–517.
53. Illingworth S, Waugh I and Juniper M. Finding thermoacoustic limit cycles for a ducted Burke-Schumann flame. *Proc Combust Inst* 2013; 34: 911–920.
54. Waugh I, Illingworth S and Juniper M. Matrix-free continuation for bifurcation analysis of large thermoacoustic systems. *J Comput Phys* 2013; 240: 225–247.
55. Gotoda H, Nikimoto H, Miyano T, et al. Dynamics properties of combustion instability in a lean premixed gas turbine combustor. *Chaos* 2011; 21: 013124.
56. Farrell BF. Optimal excitation of perturbations in viscous shear flows. *Phys Fluids* 1988; 31: 2093–2102.
57. Gustavsson LH. Energy growth of three-dimensional disturbances in plane poiseuille flow. *J. Fluid Mech* 1991; 224: 241–260.
58. Butler KM and Farrell BF. Three-dimensional optimal perturbations in viscous shear flows. *Phys Fluids* 1992; 4: 1637–1650.
59. Reddy SC and Henningson DS. Energy growth in viscous channel flows. *J Fluid Mech* 1992; 252: 209–238.
60. Reddy SC, Schmid PJ and Henningson DS. Pseudospectra of the orr-sommerfeld operator. *SIAM J Appl Math* 1993; 53: 15–47.
61. Trefethen LN, Trefethen AE, Reddy SC, et al. Hydrodynamic stability without eigenvalues. *Science* 1993; 261: 578–584.
62. Schmid PJ and Henningson DS. Optimal energy density growth in Hagen–Poiseuille flow. *J Fluid Mech* 1994; 277: 197–225.
63. Trefethen LN and Embree M. *Spectra and pseudospectra: the behavior of nonnormal matrices and operators*. Princeton, NJ: Princeton University Press, 2005.
64. Schmid PJ and Henningson DS. *Stability and transition in shear flows*. Springer Verlag, 2000.
65. Horn RA and Johnson CR. *Johnson Matrix Analysis*. Cambridge: Cambridge University Press, 1990.
66. Trefethen LN. Pseudospectra of linear operators. *SIAM Review* 1997; 39: 383–406.
67. Trefethen LN. Pseudospectra of matrices. In: Griffiths DF and Watson GA (eds) *Numerical analysis 91*. Harlow: Longman Scientific and Technical, 1991, pp.234–266.

68. Kedia S, Nagaraja S and Sujith RI. Characterizing energy growth during combustion instabilities: singularvalues or eigenvalues? *Proc Combust Inst* 2009; 32: 2933–2940.
69. Boberg L and Brosa U. Onset of turbulence in a pipe. *Z. Naturforschung* 1988; 43a: 697–726.
70. Baggett JS, Driscoll TA and Trefethen LN. A mostly linear model of transition to turbulence. *Phys Fluids* 1995; 7: 833–838.
71. Waleffe F. Transition in shear flows: nonlinear normality versus nonnormal linearity. *Phys Fluids* 1995; 7: 3060–3066.
72. Gunzburger MD. *Perspectives in flow control and optimization*. Pennsylvania: SIAM, 2002.
73. Luchini P and Bottaro A. Görtler vortices: a backward-in-time approach to the receptivity problem. *J Fluid Mech* 1998; 363: 1–23.
74. Andersson P, Berggren M and Henningson DS. Optimal disturbances and bypass transition in boundary layers. *Phys Fluids* 1999; 11: 134–150.
75. Corbett P and Bottaro A. Optimal perturbations for boundary layers subject to stream-wise pressure gradient. *Phys Fluids* 2000; 12: 120–130.
76. Schmid PJ. A general framework for stability, receptivity and optimal control. In: Wagner S, Kloker M and Rist U (eds) A general framework for stability, receptivity and optimal control. *Recent results in laminar-turbulent transition. Notes on numerical fluid mechanics and multidisciplinary design*. 2003.
77. Pringle CCT and Kerswell RR. Using nonlinear transient growth to construct the minimal seed for shear flow turbulence. *Phys Rev Lett* 2010; 105: 154502.
78. Monokroussos A, Bottaro A, Brandt L, et al. Nonequilibrium thermodynamics and the optimal path to turbulence in shear flows. *Phys Rev Lett* 2011; 106: 134502.
79. Cherubini S, DePalma P, Robinet J-Ch, et al. The minimal seed of turbulent transition in the boundary layer. *J Fluid Mech* 2011; 689: 221–253.
80. Sternberg J and Griewank A. Reduction of storage requirements by checkpointing for time-dependent optimal control probelsm in odes. In: Bücker M, Corliss G, Hovland P, et al (eds) *Automatic differentiation: applications, theory and implementations*. Springer Verlag, 2006.
81. Matsubara M and Alfredsson PH. Disturbance growth in boundary layers subjected to free-stream turbulence. *J Fluid Mech* 2001; 430: 149–168.
82. Liu Y, Zaki TA and Durbin PA. Boundary layer transition by interaction of discrete and continuous modes. *J Fluid Mech* 2008; 604: 199–223.
83. Hamilton JM, Kim J and Waleffe F. Regeneration mechanisms of near-wall turbulence structures. *J Fluid Mech* 1995; 287: 317.
84. Sharma AS, Morrison JF, McKeon BJ, et al. Relaminarisation of Re=100 channel flow with globally stabilising linear feedback control. *Phys Fluids* 2011; 23: 125105.
85. Kim J and Lim J. A linear process in wall-bounded turbulent shear flows. *Phys Fluids* 2000; 12: 1885–1888.
86. Kopitz J and Polifke W. Cfd based analysis of thermoacoustic instabilities by determination of open-loop-gain. *Twelfth international congress on sound and vibration, Lisbon*. Vol. 389.
87. Nicoud F and Wieczorek K. About the zero mach number assumption in the calculation of thermoacoustic instabilities. *Int J Spray Combust Dyn* 2009; 1: 67–111.
88. Culick FEC. Nonlinear behavior of acoustic waves in combustion chambers. Part I. *Acta Astronautica* 1976; 3: 715–734.
89. Landau LD and Lifshitz EM. *Fluid mechanics*. Oxford, UK: Pergamon, 1959.
90. George JK and Sujith RI. On disturbance energy norms. *J Sound Vibration* 2011; 331: 1552–1566.
91. Chu BT. On the energy transfer to small disturbances in fluid flow (Part I). *Acta Mech 1* 1965; 1: 215–234.
92. Myers MK. Transport of energy by small disturbances in arbitrary steady flow. *J Fluid Mech* 1991; 226: 383–400.
93. Bewley T. Flow control: new challenges for a new renaissance. *Prog Aerosp Sci* 2001; 37: 21–58.
94. Annaswamy AM, Fleifil M, Hathout JP, et al. Impact of linear coupling on the design of active controllers for thermoacoustic instability. *Combust Sci Technol* 1997; 128: 131–180.
95. Lieuwen T and Zinn BT. The role of equivalence ratio oscillations in driving combustion instabilities in low nox gas turbines. *Proc Combust Inst* 1998; 39: 1809–1816.
96. Boyer L and Quinard J. On the dynamics of anchored flames. *Combust Flame* 1990; 134: 51–65.
97. Zhao D. Thermoacoustic instability of a laminar premixed flame in Rijke tube with a hydrodynamic region. *J Sound Vibration* 2013; 332: 3419–3437.
98. Subramanian P, Wahi P and Sujith RI. Subcritical bifurcation and bistability in thermoacoustic systems. *J Fluid Mech* 2013; 715: 210–238.
99. Newell AC and Whitehead JA. Finite bandwidth, finite amplitude convection. *J Fluid Mech* 1969; 38: 279–303.
100. Stewartson K and Stuart. JT A nonlinear instability theory for a wave system in plane poiseuille flow. *J Fluid Mech* 1971; 48: 529–545.
101. Nayfeh AH and Balachandran B. *Applied nonlinear dynamics*. New York: Wiley & Sons, 1995.
102. Sujith RI, Subramanian P, Mariappan S, et al. Bifurcation analysis of thermoacoustic instability in a horizontal Rijke tube. *Int J Spray Combust Dyn* 2010; 2: 325–356.
103. Subramanian P. *Dynamical systems approach to the investigation of thermoacoustic instability*. IIT Madras, 2011.
104. Waugh IC. *Thesis title TBC*. PhD thesis, University of Cambridge, UK, 2013.
105. Sujith RI, Kabiraj L and Wahi P. Investigating the dynamics of combustion-driven oscillations leading to lean blowout. *Fluid Dyn Res* 2012; 44: 031408.
106. Kashinath K. *Nonlinear thermoacoustic oscillations of a ducted laminar premixed flame*. University of Cambridge, 2013.
107. Thampi G, Nair V and Sujith RI. Intermittency route to thermoacoustic instability in turbulent combustors. *J Fluid Mech* 2014; 756: 470–487.
108. Nair V and Sujith RI. Multifractality in combustion noise: predicting an impending combustion instability. *J Fluid Mech* 2014; 747: 635–655.